

Diplomarbeit

Compensation of thermal lensing in the GEO 600 beam splitter

Holger Wittel

Hannover, Oktober 2009

Gottfried Wilhelm Leibniz Universität Hannover
Max-Planck-Institut für Gravitationsphysik
(Albert-Einstein-Institut)

Abstract

The gravitational wave detector GEO 600 is sequentially upgraded to GEO-HF with the goal of increasing the sensitivity, especially at high frequencies, where the GEO is limited by quantum shot noise. To lower the shot noise, the upgrade will feature a laser power increase by a factor of eight. The resulting 20 kW of laser power inside the beam splitter would cause strong thermal lensing, which will substantially degrade the performance of the interferometer. Therefore a thermal compensation system for the beam splitter is essential.

The purpose and goal of this thesis was to develop, simulate and optimize a thermal compensation technique for the beam splitter in GEO 600. The compensation system is based on black body radiation, which heats the beam splitter with a defined pattern to counteract the thermal lensing. A finite element model is used to optimize the two dimensional heating flux on the beam splitter and simulate its effect. A prototype compensation system is build and evaluated with an infrared camera.

Kurzfassung

Der Gravitationswellendetektor GEO 600 wird stufenweise zu GEO-HF ausgebaut mit dem Ziel die Empfindlichkeit insbesondere bei hohen Frequenzen zu erhöhen. Dort ist die Empfindlichkeit durch Photonenschrotrauschen begrenzt. Um das Schrotrauschen zu senken, wird die Laserleistung um den Faktor acht erhöht. Die daraus resultierenden 20 kW an Laserleistung im Strahlteiler werden eine starke thermische Linse hervorrufen, welche die Empfindlichkeit des Interferometers erheblich vermindern würde. Deshalb ist ein thermisches Kompensationssystem zwingend notwendig.

Das Ziel dieser Arbeit ist es, ein Kompensationssystem zu entwickeln, simulieren und zu optimieren. Das System basiert auf thermischer Strahlung, welche den Strahlteiler in einer definierten Art und Weise erwärmt, um so der thermischen Linse entgegenzuwirken. Ein finite Elemente Modell wird benutzt um den zweidimensionalen Wärmefluss im Strahlteiler zu optimieren und den Einfluss auf die thermische Linse zu simulieren. Ein Prototyp wird gebaut und mit einer Wärmebildkamera getestet.

Contents

Abstract	i
Kurzfassung	iii
Structure	1
1 Introduction	3
1.1 Gravitational Waves	3
1.2 Gravitational Wave Detection	4
1.3 GEO 600	5
1.3.1 Recycling Techniques in GEO 600	6
1.3.2 Sensitivity & Power Up	8
1.4 GEO-HF	9
2 Thermal Effects in the Beam Splitter	11
2.1 Substrate	11
2.1.1 Thermorefractive Effect	13
2.1.2 Thermal Expansion	14
2.1.3 Flexing	15
2.1.4 Elastooptic Effect	16
2.1.5 Relative Strengths of Thermal Effects	16
2.2 Coating Effects	17
2.3 Time Dependence of the Thermal Lens	17
3 Thermal Compensation	19
3.1 Methods	19
3.1.1 Concave Lens	19
3.1.2 Shielding of the BS	19

3.1.3	Compensation Plates	20
3.1.4	IR Radiation	20
3.1.5	Cooling	21
3.1.6	Using Modes different from TEM ₀₀	22
3.2	Noise induced by the Thermal Compensation	22
3.2.1	Evaluation of the Noise caused by a CO ₂ Laser based TCS	22
3.2.2	Noise caused by a Thermal Radiation based Compensation System	24
4	Simulations	27
4.1	Introduction	27
4.1.1	The Computer Model	27
4.2	Scattering Loss as a Measure of Thermal Lensing	29
4.3	Thermal Lensing - Situation in GEO 600	30
4.4	Signal Recycling and Thermal Lensing in GEO 600	31
4.4.1	Finding the right Heating Pattern	32
4.5	Results and Discussion	35
4.5.1	Scattering Loss and focal Length	35
4.5.2	Temperatures in the BS	36
4.5.3	Misalignment of the Heating Pattern	38
4.5.4	Impact on the Interferometer	39
5	Prototype TCS	43
5.1	Requirements	43
5.2	Setup	44
5.2.1	Components	45
5.2.2	The IR Fresnel Lens	45
5.2.3	The Heating Source	46
5.2.4	Alignment and Shaping of the Heating Pattern	49
5.3	Results and Discussion	49
5.3.1	Reproducing the simulated Heating Patterns	49
5.3.2	IR Pictures and Power of the TCS	49
5.3.3	Time Dependence of the Temperature Distribution	52
6	Conclusion and future Prospects	55
6.1	Conclusion	55
6.2	Future Prospects	55

Bibliography	57
A Appendix	63
A.1 Genetic algorithm	63
A.2 ABCD Matrices to calculate the Beam Waist Size	65
A.3 Tables for the Compensation Patterns	66
A.4 Parameters for the found heating Patterns	67
A.5 Transmission Spectrum of the IR Fresnel Lens	68
A.6 Example Scripts	69
A.6.1 ANSYS Script	69
A.6.2 Example Finesse Script	72
A.7 Used Parameters	78
Acknowledgements	79
Selbständigkeitserklärung	81

List of Figures

1.1	The effect of a gravitational wave on free falling test masses	4
1.2	Simplified setup of GEO 600	6
1.3	Sensitivity curves: GEO 600 and GEO-HF	10
2.1	Geometrical situation of the beam splitter in the vacuum tank	12
2.2	Simulation of the temperature distribution in the beam splitter	13
2.3	Local thermal deformation	15
3.1	Additional noise by thermal compensation system	25
4.1	Finite elements model of the beam splitter	28
4.2	Work flow for the simulation	29
4.3	Optical path difference for GEO 600 and ideal lens approximation	31
4.4	Comparison of signal recycling mirrors transmittances of 2 and 10 percent and the case of no SR mirror	33
4.5	Variables of the heating pattern	34
4.6	Optical path difference cross sections in x (horizontal) and y (vertical) direction for the compensated and uncompensated case of a 20 kW laser	36
4.7	Scattering loss in dependence of the power of the thermal compensation system for the narrow pattern.	37
4.8	Temperature distribution for different heating patterns in the BS. The temperatures are color coded and show the temperature in K, an ambient temperature of 300 K is assumed.	37
4.9	Performance for 2 different misaligned heating patterns	38
4.10	Comparison of circulating power and the PRC gain of GEO with and without thermal compensation	40
4.11	Comparison of the darkport power and the ratio of darkport power to circulating power in GEO with and without thermal compensation	41

5.1	Schematic setup of the TCS prototype system, viewed from above	44
5.2	Photo of the actual TCS prototype system	45
5.3	Photograph of the heating wire	46
5.4	Absorption spectrum of fused silica	47
5.5	Temperature of the heating wire for different electrical powers	48
5.6	Possible heating pattern shapes	50
5.7	Central heating of the BS	51
5.8	Thermography and simulation of the temperature on the heated BS face	53
5.9	Temperature profile of the heated beam splitter front in horizontal direction . .	54
5.10	Temperature variation over time	54
A.1	Visualization of the working principle of a genetic algorithm	64
A.2	Transmission spectrum of the IR Fresnel lens	68

Structure

The following paragraphs provide a quick overview of this thesis.

In **chapter 1** I give a brief introduction into gravitational waves and the efforts made to directly detect them using interferometric detectors. This includes a rough description of the interferometers using GEO 600 as an example detector. Additionally, the upgrades to GEO-HF are mentioned.

Chapter 2 describes possible thermal effects that may arise in the beam splitter and gives an introduction into thermal issues regarding gravitational wave detectors and thermal lensing. Since this work focuses on the GEO 600 beam splitter, it is explicitly described in more detail. Also, the current thermal lensing situation in the GEO 600 beam splitter is elaborated.

Chapter 3 lists the different possibilities of compensating the thermal lensing effect and justifies the approach taken in this work. The additional noise added by the thermal compensation system is calculated.

Chapter 4 focuses on the simulations of the beam splitter and the interferometer. It provides a comparison of the simulations with an analytical model of thermal lensing.

In **chapter 5**, a prototype of the thermal compensation system is described and characterized. The result of this prototype system are then compared to the simulations carried out in the previous chapter.

Finally, **chapter 6** provides an outlook and a conclusion.

The **appendix** provides an explanation of the genetic algorithm, which was used in the simulations. It also incorporates an example script for the finite elements software ANSYS, which was used to determine the temperature distribution inside the beam splitter. A sample script for the interferometer simulation software FINESSE is also given. It was used to determine the effect of the thermal lensing and the thermal compensation on the interferometer. An ABCD matrix calculation of the beam waist size in the beam splitter follows. Finally, a table shows the different parameters and their values which were used in this thesis.

Chapter 1

Introduction

1.1 Gravitational Waves

Einstein's general theory of relativity changed our perception of space and time. One of its predictions is the presence of gravitational waves. Gravitational waves (**GW**) can be described as “[...] propagating oscillations of the gravitational field [...]”([BS09]). The oscillations arise from the acceleration of massive objects: They can occur as one big event, like a non symmetrical supernova, or as constant emission of gravitational energy, like in coalescing binary star systems. GW propagate with the speed of light. While they propagate, they affect the relative position of free falling test masses in directions perpendicular to their direction of propagation. This is visualized in fig. 1.1. For a proper introduction into the general theory of relativity and gravitational waves I'd like to point the reader to [MTW⁺73], [Sch03] and [Sch09].

So far, gravitational waves have only been detected indirectly. This was possible by the discovery of the pulsar B1916+13, the first one in a binary system ([HT75a]) and the observation of its pulse rates. Pulsars are stellar objects that emit electromagnetic radiation at very regular time intervals. In the case of B1916+13, a shift in the pulse rates was observed. The explanation is that the orbit of the pulsars is decaying due to a loss of energy. The amount of lost energy is in perfect agreement with the energy loss due to emission of gravitational waves, as predicted by the general theory of relativity. For the discovery of this remarkable “space-laboratory” Hulse & Taylor were given the Nobel Price in 1993.

The long term goal of the GW community is to do astronomy with GW. It would open a completely new window of “looking” into space. GW do not interact easily, unlike electromagnetic radiation which suffers from absorption and gravitational lensing. Another aspect that makes GW interesting for astronomy is that the universe was opaque for EM radiation in the

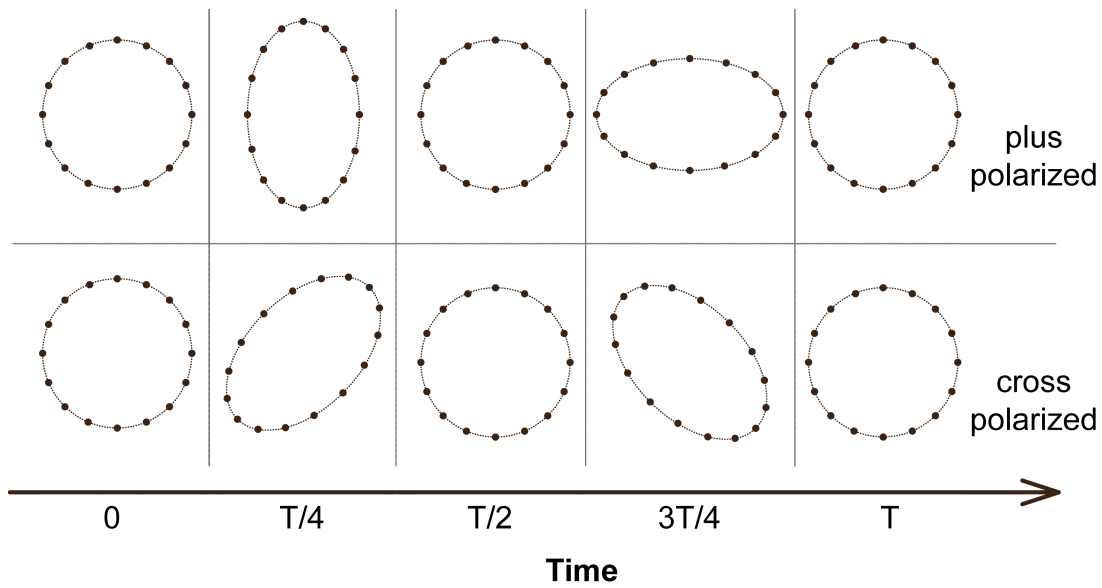


Figure 1.1: The effect of a gravitational wave on free falling test masses for the two possible polarizations are pictured. In this case, the direction of propagation is perpendicular to the paper plane.

first 300000 years after the Big Bang. Which means it is not possible to investigate the very beginning of the universe with optical telescopes. A telescope for gravitational waves would not suffer this limitation, and could look back in time much further. For making such observations, it is of course necessary to detect GW first. The difficulty lies in the fact that the effect of GW is extremely small. The strain caused by a gravitational wave is defined as the length change δl per length l . The amplitude of the GW is defined as $h = 2\frac{\delta l}{l}$. The strain caused by the strongest gravitational waves arriving on Earth is expected to be smaller than 10^{-21} , on a scale of 1 km that would mean a length change of 10^{-18} m, or approximately one thousandth of a proton diameter.

1.2 Gravitational Wave Detection

For gravitational wave astronomy it would be necessary to detect gravitational waves directly. Different approaches of detecting them are being followed, in order to make it possible to detect gravitational waves of different frequencies.

The method detecting the lowest frequency GW is called “pulsar timing”. Pulsar timing works by observing the pulse delays of many pulsars in different directions. A deviation in the pulse arrival times might be caused by a passing GW that changed the distance between the pulsars and Earth. Pulsar timing probes gravitational waves with frequencies of nano Hz.

Another approach is to build a device that detects gravitational waves directly, called gravitational wave detector (**GWD**). There are two kinds of GWD in use today, those that employ resonant bars, and those that use interferometers. Developed in the 1960s, resonant bar-detectors were the first kind of GWDs. They consist of a cryogenically cooled metal bar or a sphere, mostly aluminum, in the range of 2 tons. If a gravitational wave passes, it would excite a resonant mechanical mode in the bar. The vibrations would then be measured. These detectors are sensitive for a narrow bandwidth of approximately 50 Hz at frequencies in the range of 700 – 900 Hz. The third method of detecting gravitational waves utilizes laser interferometers. Today, this kind of detection is the most sensitive, and on Earth it works best for gravitational waves with frequencies of one hundred Hz to a few kHz.

Spaceborne interferometric detectors like LISA ([Sha08]) will be sensitive for GW with frequencies of mHz up to 1 Hz and fill the gap between ground based detectors and pulsar timing.

In this work I want to focus upon the interferometric gravitational wave detectors. There are several kilometer-scale projects using interferometers (**ifo**), namely GEO 600 ([G⁺08]), LIGO ([K⁺08]), VIRGO ([AAA⁺08]) and TAMA ([TAT⁺08]).

1.3 GEO 600

This section gives a description of interferometric GWDs, based on the example of the German-British detector GEO 600. A much more detailed introduction on interferometric gravitational wave detectors can be found in [Sau94].

All long-scale GWDs are Michelson interferometers with arm lengths in the range of several 100 meters to kilometers. The concept of a Michelson ifo is suited very well for the sensing of GW, because it is sensitive to the differential arm length changes that are induced by GW. The mirrors of the interferometer are suspended as a pendulum, and can be considered as free falling mass in the direction of the optical axis. Thus, a passing gravitational wave changes the length of the interferometer arms: one arm would be stretched while the other arm would be shortened, which leads to a modulation of the light power in the output of the interferometer. Ground based GWD have the best sensitivity for gravitational waves at frequencies in the range of 100 Hz to 1 kHz. At higher frequencies shot noise is a limiting factor, while thermal and seismic noise limit the sensitivity at lower frequencies. In the case of GEO 600 the physical arm-length is 600 meters. However the arms are folded once, so that the total optical path is 1200 meters in each arm. Other detectors use arm cavities, which have the effect of folding the arms and therefore increase the optical arm length. The laser used in GEO 600 is a 10 W Nd:YAG laser with a wavelength of 1064 nm. A simplified setup of GEO 600 is shown in

fig. 1.2. To minimize unwanted noise, the whole interferometer is set up in a vacuum system. Additionally, beam splitter and mirrors are hanging on pendulum suspensions to decrease the influence of seismic noise.

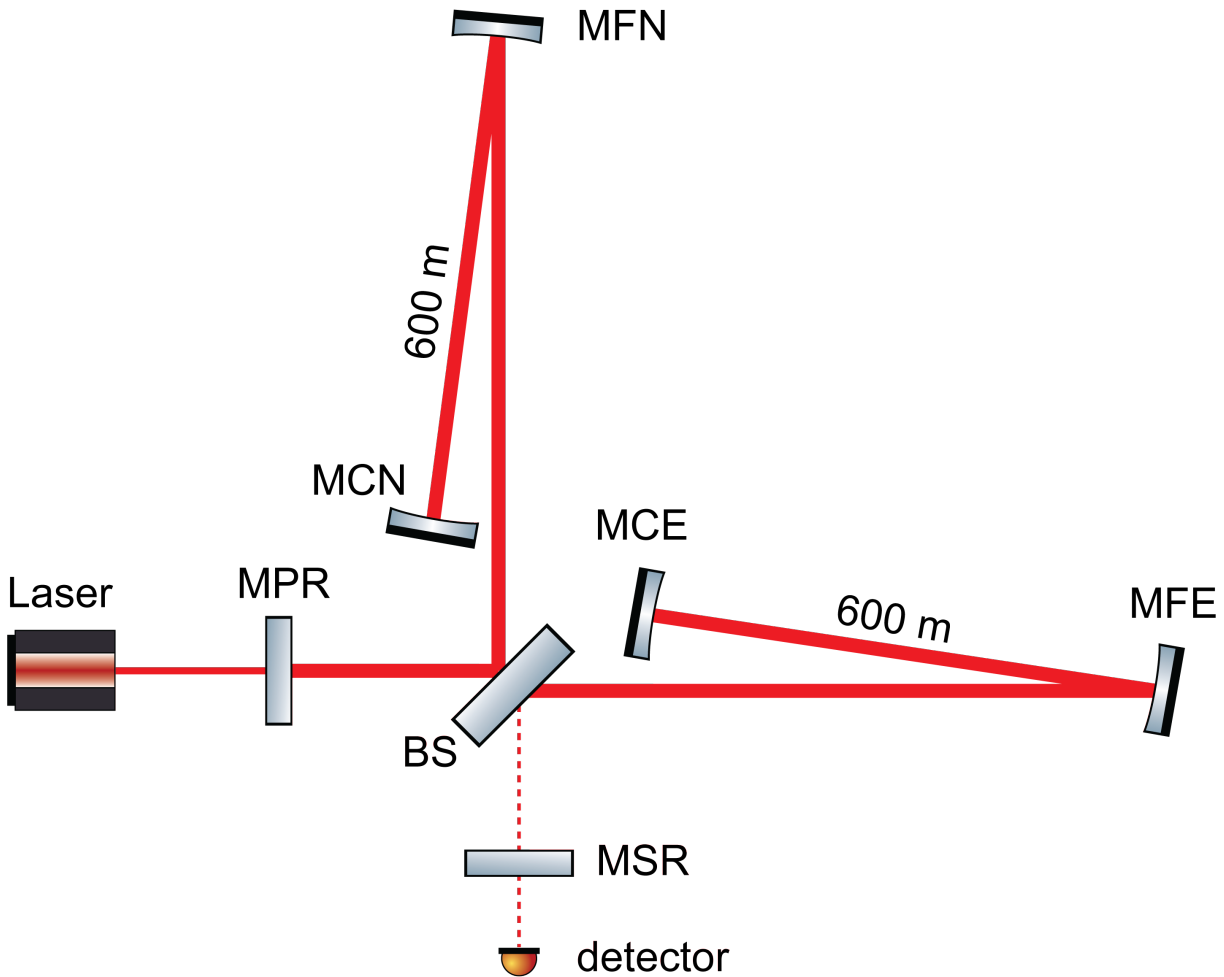


Figure 1.2: Simplified setup of GEO 600. BS denotes the beam splitter, MSR the signal recycling mirror, MPR the power recycling mirror. MFE and MCE are the far east- and central east mirror. The notation for the north arm is analogue.

1.3.1 Recycling Techniques in GEO 600

GEO 600 uses two recycling techniques: power recycling and signal recycling. Both have an impact on the power circulation inside the ifo and on the thermal lensing, therefore I want to give a short description of each of this techniques.

Power Recycling

Power recycling (**PR**) is used by all big ifo GWD projects. The purpose of this technique is to enhance the circulating power in the interferometer. Starting from a simple Michelson interferometer, the implementation is done via operating the interferometer at the dark fringe, so that the output is dark: All the light is reflected back to the input port. Then a mirror is added to the input of the interferometer to reflect this light back again. This way a resonant cavity is formed between the power recycling mirror and the arm end mirrors, called the power recycling cavity (**PRC**). It can cause a high power build up in this cavity. In the case of GEO 600 the power build up reaches nearly a factor 1000.

Signal Recycling

Signal recycling (**SR**) is an advanced interferometer technique, currently only used by GEO 600 ([HGH⁺07]). It will be implemented in future detectors like Advanced LIGO ([Mue08]) and Advanced Virgo ([Col07]). The concept is similar to the power recycling: a mirror is put to the darkport of the interferometer, to enhance the signal, which would be produced by a gravitational wave. It can increase the shot noise limited sensitivity in a certain frequency range and be used to shape the shot noise curve. It might seem counterintuitive that a mirror at the darkport would have any influence on the interferometer, but it does have a big impact on its performance. The signal recycling mirror forms a resonant cavity with the arm end mirrors, the signal recycling cavity (**SRC**). Three modes of operation are possible, depending on the exact position of the SR mirror: tuned SR ([HGH⁺07]), detuned SR([HGH⁺07]), and resonant sideband extraction ([MSN⁺93]).

A nice overview of these techniques is given in [FHS⁺00]. Within this thesis, only the second benefit of SR will be considered: It causes mode healing ([GFM⁺04], [FHS⁺00]). It has a positive effect on the high order mode content at the output and inside the interferometer, can therefore improve the thermal lensing situation and the circulating laser power as well as the output contrast. A closer look on the effect of signal recycling on the thermal lensing is given in chapter 4.4. For the current laser power, the SR also shows an impact on the circulating laser power. It shows if the interferometer is operated as a power recycled Michelson by misaligning the SR mirror by about $10 \mu\text{rad}$, then the circulating laser power drops by about 40%. In conclusion it can be stated that signal recycling does have an effect on the circulating power.

1.3.2 Sensitivity & Power Up

Since GWD aim to detect very small displacements, the quantum nature of the used laser-light has to be considered. The sensitivity of an ifo GWD depends on several parameters and noise sources and is difficult to predict exactly. Therefore I want to consider the case of a simple Michelson interferometer operated at a half fringe to point out that the achievable sensitivity depends on the circulating light power. The sensitivity for a simple Michelson interferometer is ultimately limited by the standard quantum limit (SQL), which is the sum of radiation pressure noise and shot noise. Both arise from the quantum nature of light: Light consists of photons with a Poisson distribution.

- **radiation pressure noise**

The photons carry momentum. When they are reflected by a mirror, they apply a force on it. Since the number of photons arriving at the mirror at each time interval is not constant, the mirror is shaken by the photons. This is called the radiation pressure noise. Translated into strain noise, the pressure noise can be quantified as $h_{rp} = \frac{1}{m f^2 L} \sqrt{\frac{\hbar P_{in}}{2\pi^3 c \lambda}}$.

- **shot noise**

When operating a Michelson interferometer, the quantity which is detected is the brightness change at the output of the interferometer. There is noise in the brightness of the output as well, again due to the counting statistics of the photon arrival times. The impact of shot noise on the strain sensitivity can be quantified as $h_{shot} = \frac{1}{L} \sqrt{\frac{\hbar c \lambda}{2\pi P}}$,

where L is the optical length, m the mirror masses, λ the laser wavelength and P the laser power in the interferometer arms. c denotes the speed of light. This formulas shows the relation between the parameters L , P , λ and the sensitivity. For today's interferometers, which are optimized for frequencies in the range of 100 Hz to 1 kHz, the radiation pressure noise, which scales with $1/f^2$ can be neglected. At the moment GEO 600 is shot noise limited for frequencies above 1kHz.

However, the case of GEO 600 is more complicated. It uses SR, and will be implementing squeezing. Both techniques can beat the SQL ([HCC+03]). Still the shot noise formula above gives the right dependencies between the sensitivity and the different parameters. As can be seen from the shot noise formula, the sensitivity of the interferometer is determined by the arms length, the wavelength of the laser and the circulating power. The first two options are hard to improve, since the arm length of the existing interferometers can not be changed easily. Also lasers of shorter wavelengths with sufficient power and stability have to be developed first. Increasing the light power is the best option to increase the sensitivity of a shot noise limited Michelson interferometer. This is done by using strong lasers, and using power recycling

techniques. High laser powers induce thermal problems though, like described in the next chapter, especially in transmissive optics.

1.4 GEO-HF

By the time of writing this thesis, the transition from GEO 600 to GEO-HF (HF = high frequency) has already started. GEO-HF will continue to explore new technologies. The goal is to increase the sensitivity by a factor of eight over GEO 600, while shifting the sensitivity maximum to a higher frequency of 1 kHz.

The upgrades to the original GEO 600 detector include:

- squeezing
squeezed vacuum states of light will be injected to improve the sensitivity in the high frequency regime by lowering the shot noise ([Vah08]).
- the installation of an output mode cleaner, to lower the contribution of higher order modes to shot noise ([DGP⁺]) at the output.
- an increase of the circulating light power to ≈ 20 kW.
this will be achieved by a stronger input laser with 35 W and new input mode cleaner mirrors with higher transmittance.
- a new broadband signal recycling mirror,
it will broaden the region of best sensitivity.
- the installation of a thermal compensation system to counteract thermal lensing in the beam splitter, which is the topic of this work.

The expected sensitivity gain can be seen in fig. 1.3. It shows the current sensitivity, as well as the improvements due to squeezing, a new signal recycling mirror and the power increase. The sensitivity will be improved at all frequencies, but the largest improvement is expected for frequencies higher than 1 kHz. Since the upgrade to GEO-HF has already started and big parts of this work apply to both GEO 600 and GEO-HF, I will often just refer to the detector as “GEO” in these cases.

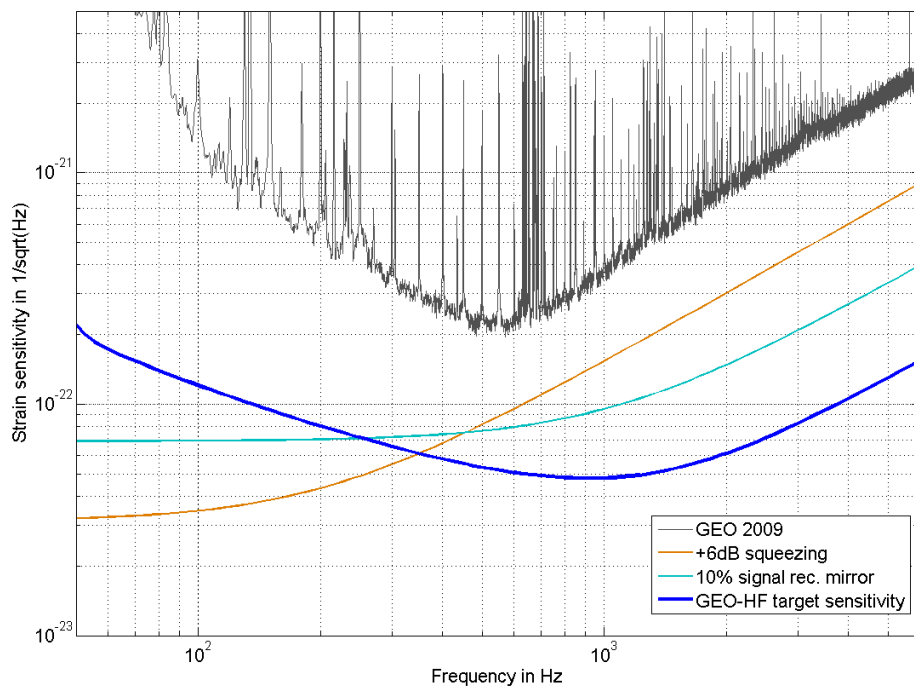


Figure 1.3: Sensitivity curves: The sensitivity of GEO 600 and the expected sensitivity of GEO-HF are shown, as well as the sensitivities for some intermediate steps to the final GEO-HF.

Chapter 2

Thermal Effects in the Beam Splitter

The study of thermal effects in interferometric gravitational wave detectors is still ongoing work. Nonetheless I want to give a short introduction on several thermal effects in the GEO 600 beam splitter (**BS**), which will also be used in GEO-HF. Thermal effects also happen on other optics of GEO, but the beam splitter is of particular interest, since it is a transmissive element. Because GEO has no arm cavities, the beam splitter is placed at the location with the highest light intensity within the interferometer. This can lead to thermal issues, which I want to describe in this chapter.

The beam splitter of GEO 600 is made from fused silica (Suprasil 311 SV). It is cylindrical with a diameter of 26 cm and a thickness of 8 cm. It has a mass of approximately 9.3 kg and features a very low absorption at 1064 nm, measured to be 0.25 ± 0.1 ppm/cm ([HLW⁺06]), but recent results point to an absorption closer to 0.4 ppm/cm ([Hil09]). Since the absorption is not exactly known, I used a value of 0.5 ppm/cm for the absorption in the beam splitter. On the one side, the BS has coating with 52 % transmittance and 48 % reflectivity, the other side is anti-reflective (**AR**)-coated. The geometical situation of beam splitter and laser beam in the vacuum tank is presented in fig. 2.1.

The thermal effects can be separated into 2 groups: coating thermal effects and thermal effects within the substrate. The sum of the thermal effects is called “thermal lensing.”

2.1 Substrate

In the horizontal plane, the laser beam passes the beam splitter at an angle of about 43 °. With Snell’s law and a refractive index of about 1.45 it follows that the angle inside the beam splitter is 28 °. It follows that the physical path length inside the BS is about 9 cm. The light power

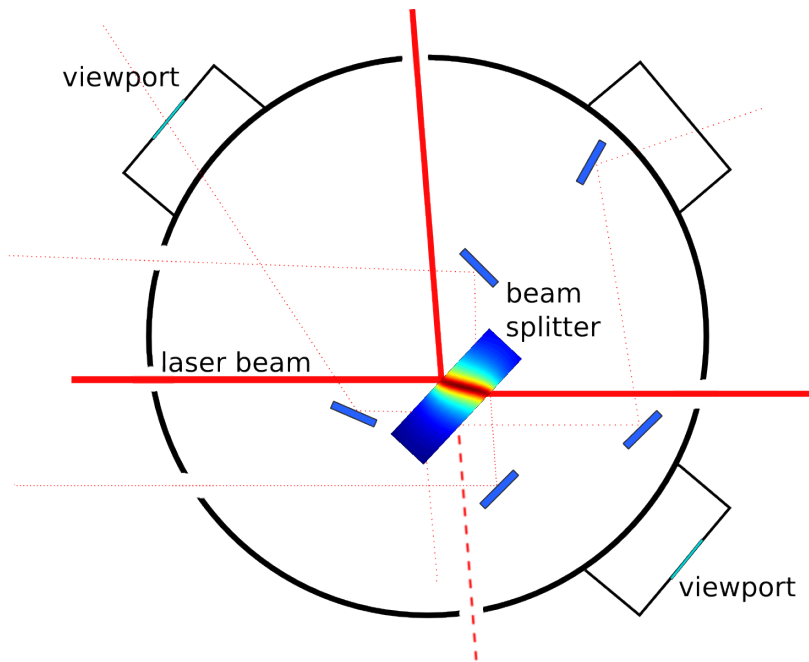


Figure 2.1: Approximate geometrical situation of the beam splitter in the vacuum tank. The power recycling mirror would be to the left. The dashed red line represents the darkport output of the interferometer. The dotted lines are pickup beams for diagnostical and control purposes from the beam splitter.

coming from the power recycling mirror is about 2.7 kW. Half of that power is reflected into the north arm, the other half passes the beam splitter. The light that passed the BS is then reflected back to the beam splitter via the east end mirror. The reflected light field overlaps with the incoming one, therefore the light power in the beam splitter that is relevant for the absorption is 2.7 kW. With an absorption of 0.5 ppm/cm follows a generated heat of 12 mW in the BS for the current power level. That leads to a temperature increase of 0.048 K along the optical path¹. The choice of a good substrate material is critical for thermal effects. As of today, all big GWDs use fused silica optics, which is available in very low absorption versions. Sapphire is planned to be used in the cooled future high power detector LCGT ([Kur06]). It is not available with absorptions as low as the fused silica, but since it has a much better thermal conductivity, the temperature gradient will be lower.

¹The temperature increase has been computed by finite element simulations, fig. 2.2 shows the laser-induced temperature increase in the BS

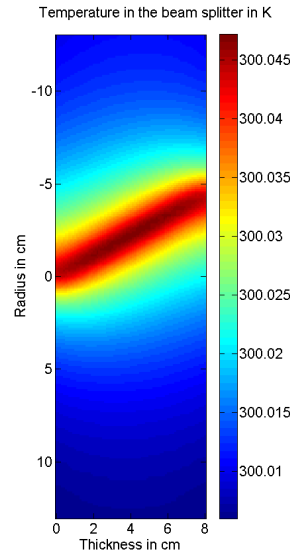


Figure 2.2: Simulation of the temperature distribution in the BS with a surrounding temperature of 300 K.

2.1.1 Thermorefractive Effect

The strongest effect in fused silica is due to the temperature dependency of the refractive index. The thermorefractive coefficient $\beta = \frac{dn}{dT}$ describes the temperature dependence of the refractive index n . For fused silica this coefficient is positive, meaning that the optical path gets longer the higher the temperature along this path is. This is what happens in the BS: the laser heats up the BS along the optical axis, causing a higher refractive index there. The profile of the refractive index will be proportional to the intensity profile of the laser. This causes the optical path to be longer on the optical axis than off the axis, similar to what a thin lens causes. Like an ideal thin lens, the thermal lens can also be described by its focal length. With the following simple model one can calculate the focal length: Assuming only radial heat flow and uniform bulk absorption, the radial temperature $T(r)$ can be described as ([SDM⁺94]):

$$T(r) = \frac{P p_{abs}}{4\pi\kappa} \sum_{n=1}^{\infty} \left(2 \frac{r^2}{w^2} \right)^n \frac{(-1)^n}{nn!}, \quad (2.1)$$

Here w is the beam waist size, r the radial distance from the optical axis, p_{abs} the fraction of light absorbed per unit length and P the light power.

A simplification: for the thermal lensing, one can take into consideration only the temperature difference between $r = 0$ and $r = w$, then the series for $r = w$ gives a factor of

1.32:

$$\Delta T = T(0) - T(w) = 1.32 \frac{P p_{abs}}{4\pi\kappa} \quad (2.2)$$

The temperature difference ΔT transforms to an optical path difference (**OPD**) by multiplication with the thermo-refractive coefficient β and the path length L in the substrate:

$$\Delta OPD = \Delta T \beta L = 1.32 \frac{P p_{abs} L \beta}{4\pi\kappa} \quad (2.3)$$

With $f_{therm-model} = w^2 / (2 \cdot \Delta OPD)$ the focal length of the thermal lens of the substrate can be expressed as

$$f_{therm-model} = \frac{4\pi}{2 \cdot 1.32} \frac{w^2 \kappa}{\beta L P p_{abs}} \quad (2.4)$$

When calculating the focal length it needs to be considered that the beam waist is different in the horizontal (x) and vertical (y) direction, as shown in appendix A.2. It follows

$$f_{therm-model-x} = 8.8 \text{ km} \quad (2.5)$$

$$f_{therm-model-y} = 6.2 \text{ km} \quad (2.6)$$

with the following values used: thermal conductivity $\kappa = 1.4 \text{ W/mK}$, the beam radius $w_x = 1.2 \text{ cm}$, $w_y = 1 \text{ cm}$, the substrate absorption $p_{abs} = 0.5 \text{ ppm/cm}$, the thermo refractive coefficient $\beta = 9 * 10^{-6} \text{ K}^{-1}$, the laser power $P = 2700 \text{ W}$ and the path length inside the BS $L = 9 \text{ cm}$.

2.1.2 Thermal Expansion

A second known thermal effect is the deformation of the substrate. The substrate heats up locally along the path of the laser beam. This causes the material to expand, making the physical (and therefore optical) path longer. The material can only expand at the surface of the BS, since the heated region inside the BS is held in its position by the surrounding colder part of the substrate. The result is a local “buckling” of the front and back surface. With a simple model like in [MHG⁺01], only the heat flow in a half sphere with the waist radius of the laser is considered. This yields the optical path difference for the local deformation at the front and back side of the BS as:

$$\Delta OPD_{expansion} = 2\alpha n w \Delta T, \quad (2.7)$$

α is the thermal expansion coefficient. With the ideal lens approximation $f = w^2/(2 \cdot \Delta OPD)$ the strength of the thermal expansion effect can be expressed as a focal length:

$$f_{expansion} = \frac{w}{4\alpha n \Delta T} \quad (2.8)$$

$$f_{expansion-x} \approx 371 \text{ km} \quad (2.9)$$

$$f_{expansion-y} \approx 310 \text{ km} \quad (2.10)$$

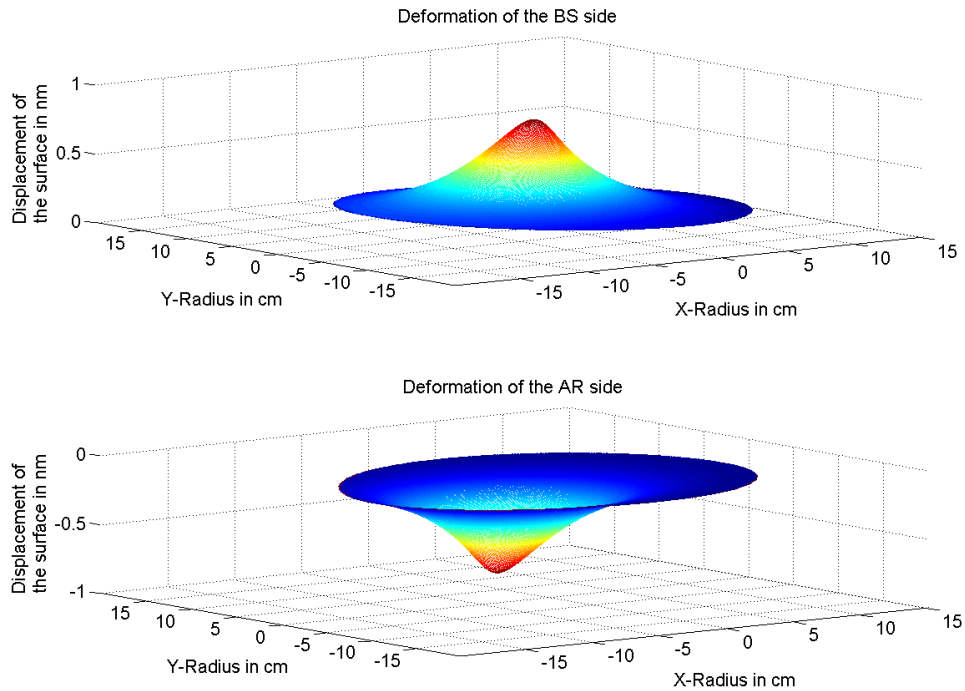


Figure 2.3: Simulation of the local thermal deformation, please note that the z-axis scaling is set to nanometers, to make the deformation effect visible.

2.1.3 Flexing

Another thermal effect that needs to be considered is the so called “flexing.” This only needs to be considered in the case that only one side of the BS is heated, e.g. by a thermal compensation system. It causes the BS to bend like a meniscus lens. This kind of thermal compensation is already used in GEO to compensate for a wrong radius of curvature in the east arm mirror ([LFG⁺04]). The mirror is heated from the back, which causes bending of the whole mirror and a change in the radius of curvature.

2.1.4 Elastooptic Effect

The last thermal effect mentioned here is the elastooptic effect: The heating on the optical axis causes stress to the material. The refractive index of fused silica also depends on stress, therefore the optical path length is influenced by the stress as well. For isotropic materials like fused silica, the optical path difference can be approximated ([MHG⁺01]) as:

$$\Delta OPD_{elastic} \approx -\frac{n^3}{2} \rho_{12} \alpha L \Delta T \quad (2.11)$$

The corresponding focal length for the current laser power is:

$$f_{elastic} = \frac{-w^2}{n^3 \rho_{12} \alpha L \Delta T} \quad (2.12)$$

$$f_{elastic-x} \approx -349 \text{ km} \quad (2.13)$$

$$f_{elastic-y} \approx -242 \text{ km} \quad (2.14)$$

Here ρ_{12} is the photoelastic coefficient.

2.1.5 Relative Strengths of Thermal Effects

This section compares the relative influence of the different effects on the optical path length. Table 2.1 presents the optical path differences caused by the different thermal effects. The values are calculated by making use of the formulas presented above, using the parameters for the GEO 600 beam splitter, which can be found in table A.6. The thermorefractive effect is by far the dominating term. Other effects that can cause an optical path length change can be safely neglected. The focal length of the thermal lens after the power upgrade will be presented in chapter 4.3.

Effect	$\Delta OPD/\Delta T$ (m/K)	relative strength
thermorefractive	$8.1 \cdot 10^{-7} \Delta T$	1
thermal expansion	$1.6 \cdot 10^{-8} \Delta T$	0.02
elastooptic	$-2 \cdot 10^{-8} \Delta T$	-0.025

Table 2.1: Comparison of the relative strengths of thermal effects in the beam splitter. Only the values in the vertical (y) direction are compared here.

2.2 Coating Effects

The absorption in the optical coating of the GEO BS has not been measured. Since coatings with absorptions lower than 1 ppm are available, it can be assumed that the BS meets that value, especially when considering that the BS-side coating has only 4 layers. Compared to the substrate absorption of $0.5 \text{ ppm/cm} \cdot 9 \text{ cm} = 4.5 \text{ ppm}$, the coating effects play only a minor role in terms of thermal lensing. Therefore they have been neglected in this work.

2.3 Time Dependence of the Thermal Lens

It takes some time for the thermal lens to reach a steady state. Following [Bal06], the time constant for the formation of the thermal lens can be approximated as

$$\tau_{lens} = \frac{C\rho \cdot (\text{heated Volume})}{(\text{conductive cooling rate})} = \frac{C\rho\pi w^2 L}{2\pi\kappa w} \approx 10 \text{ min.} \quad (2.15)$$

The variables used here are given in table A.6. This equation describes only the heat flow within the substrate by heat conduction. It gives an approximation for the time constant of the relative temperatures in the BS. For the absolute temperature scale the radiative cooling of the BS determines the time until it reaches a thermal equilibrium. The time constant for the BS to reach a thermal steady state is:

$$\tau_{BS} = \frac{Cm_{BS}}{(\text{radiative cooling rate})} = \frac{Cm_{BS}}{4A\sigma T_0^3} \approx 2 \text{ hours.} \quad (2.16)$$

It shows that the thermal lens forms much quicker than the overall thermal relaxation time. This is also relevant for a thermal compensation system. This work will focus mainly on thermal steady states, especially the simulations in chapter 4. The thermal relaxation time is important for a thermal compensation system though, especially when designing a control system for the thermal compensation system.

Chapter 3

Thermal Compensation

3.1 Methods of Thermal Compensation

There are different ways to achieve a thermal compensation effect. In this chapter I want to give an overview of the possibilities.

3.1.1 Concave Lens

The most obvious way to compensate for thermal lensing is by using a concave lens with a focal length chosen to correct for the thermal lens. This simple method is sometimes seen in high power solid state lasers, which use a convex mirror for that purpose. This method has disadvantages: Since the thermal lens has a focal length in the order of kilometers, the lens would have to have the same focal length, but with the opposite sign. For a good compensation it would have to be an aspheric lens with a focal length in the range of kilometers. Since the lens would be passed by the laser beam itself, it would introduce its own thermal lens, which needs to be considered. With the additional lens the interferometer would be over-corrected when cold - which makes the locking process harder, if not impossible without an additional heating. The addition of a compensating lens is not a very flexible solution, because the optimal compensation is only achieved for one specific circulating power. Another negative aspect is that with additional transmissive optics, an additional loss is induced.

3.1.2 Shielding of the BS

In order to reach a more homogeneous temperature profile in the BS, a shielding that prevents thermal radiation from leaving the BS could be added. The purpose of this “radiation shield”

would be to reflect thermal radiation that would otherwise leave the BS. This could be especially useful at the sides of the BS. The radiation shield could consist of a gold foil at a close distance to the BS. Another way to realize a radiation shielding could be a coating with a low emissivity. This way, a more even temperature profile may be realized. The GEO 600 beam splitter has been installed without a radiation shield, and an afterward installation would prove to be a difficult task. The effect of a radiation shield for the GEO 600 BS has been simulated and found to be minimal. This could be expected, since the BS is thin, its radius is larger than its thickness. The temperature at the outer radial edge of the beam splitter does not affect the center much.

3.1.3 Compensation Plates

A compensation plate is a window of transmissive material, like fused silica, which is inserted into the path of the beam. To correct for thermal lensing, compensation plates can be used in two different ways:

1. Placed in the north arm,
it would make the situation in the interferometer arms symmetrical, since it would induce its own thermal lens. If the probe beam is changed the same way in both arms, a good destructive interference at the darkport could still be realized.
2. Placed in the east arm,
it could be used with a heating to counteract the thermal lens in the BS. The purpose of the heating is to create a thermal lens in the compensation plate that is inverse to the one in the BS. This can be done by an annular heating of the compensation plate.

An inverse thermal lens to the one in the BS can also be achieved by using a compensation plate made from a material with a negative thermorefractive coefficient.

As additional transmissive optics, compensation plates would also add additional loss.

3.1.4 IR Radiation

Infrared (**IR**) radiation can be used to heat up the optics or a compensation plate in order to compensate for the thermal lensing. Only IR radiation with wavelengths longer than $2.5 \mu\text{m}$ is absorbed significantly in the GEO beam splitter. Several ways of applying the IR radiation to the BS exist:

A ring heater is a ring shaped heating device inside the vacuum tank, near the optics. It is used to heat either a compensation plate or the optics directly in an annular way through IR radiation. In GEO, spacial restrictions make the use of a ring heater for heating the BS difficult.

Heating using IR radiation from outside can be used. It has the benefit that the heating can be easily accessed, without opening the vacuum tank. This method requires an IR transmissive vacuum viewport in the right place. Fortunately, two viewports are available in GEO at either flat sides of the BS. The heating with a CO₂ laser is already implemented for the LIGO arm cavity input mirrors ([A⁺09]).

A thermal source can also be used as a source of infrared light, as we will see later. It is more convenient than a laser, cheap, reliable and induces potentially less noise. The thermal radiation based TCS cannot as powerful as a CO₂ laser though. However, for the case of GEO that poses no problem. Only a low powered thermal compensation system (TCS) will be needed for GEO-HF, as the simulations in the next chapter will show.

3.1.5 Cooling

Another method of dealing with the thermal lens is cooling the optics. This approach is tested in LCGT. Cryogenical cooling of the entire optical setup might be a solution for future detectors. The thermal conductivity of many materials, including fused silica and sapphire improves at lower temperatures, therefore the thermal lensing would be weaker. However, for cooling the optics, sapphire would be a much better material than fused silica ([DZJB06]).

A second method of thermal compensation through cooling is the so called radiative cooling ([JKKPD09]). This method uses a small cold (possibly liquid nitrogen cooled) target, which is projected on a point of the optic using big mirrors. With a setup like this, the selected spot on the optics will “see” the thermal radiation of the cooled target instead of the normal room-temperature background. As a result, the optics will be cooled on the selected spot. This would allow the selective cooling of a specific spot on the optics. In theory this method could be used for compensating the thermal lens. Whether it is really suited for the GEO beam splitter or not is calculated in the following section.

Estimation for GEO 600

With a beam waist radius of approx 1 cm, the area to be cooled on the BS is $A = \pi w^2 \approx 3 * 10^{-4} \text{ m}^2$. The radiated thermal power emitted by this area of the BS can be calculated by the Stefan-Boltzmann law: $E_{rad} = \sigma \epsilon A T_0^4 \approx 0.14 \text{ W}$. This 0.14 W account for $\frac{300^4 \text{ K}^4 - 77^4 \text{ K}^4}{300^4 \text{ K}^4} \approx 99.6\%$ of the radiation between the BS and the target if areas of the same size are assumed. The radiation emitted by the target can therefore be neglected.

The power of 0.14 W is emitted into the solid angle of 2π . The emitted power per steradian is $E_{sr} \approx 0.02 \text{ W/sr}$. Now the mirrors that direct the radiation from the hot spot on the BS towards the target come into play. A bigger covered solid angle is better for the cooling power.

Concerning this, there are some restrictions, e.g. lack of space: the laser must not be blocked, as well as pickup beams coming from the BS. If we assume mirrors that cover a solid angle of one quarter of the half space, or 0.5π , the maximum cooling power would be $0.02 \text{ W/sr} \cdot 0.5\pi \cdot 2\text{sides} \approx 0.06 \text{ W}$.

The cooling needs to be able to compensate for the absorbed laser power inside the BS which is approx 12 mW for the current power. With a power update of a factor 8 in mind, one can see that the radiative cooling method would not be sufficient. Even with one whole half space covered with mirrors, the maximum cooling power would be just a bit more than the expected 100 mW of absorbed power. But there are still no losses included, nor is there enough space in the GEO vacuum tank to implement large mirrors.

3.1.6 Using Modes different from TEM₀₀

One other method of getting around the thermal issues is not to use the TEM₀₀ mode for the probe laser beam. For example one could use a high-order Laguerre-Gauss mode, or a “flat top” beam. That would have the benefit of having a more evenly distributed and more wide-spread light intensity profile, thus reducing thermal effects. Especially the thermorefractive effect, which depends quadratically on the beam radius, could be reduced. This method has been suggested by several authors like Vinet in [Vin09].

3.2 Noise induced by the Thermal Compensation

Since the thermal compensation system is planned to act directly on the BS, it might add additional noise. This section will give an estimate of the additional noise caused by a thermal compensation system.

3.2.1 Evaluation of the Noise caused by a CO₂ Laser based TCS

I want to evaluate how much the relative intensity noise RIN of a CO₂ laser based thermal compensation system would affect the sensitivity of GEO 600. There are several effects contributing to the noise: the radiation pressure, the refractive index change, the thermal expansion and the flexing of the beam splitter. The formulas are taken from Stefan Ballmer’s PHD thesis ([Bal06]).

The radiation pressure displacement noise is given by

$$\delta l_{RP}(f) = RIN \frac{\langle P_{abs} \rangle}{mc(2\pi f)^2} \approx 3.64 \cdot 10^{-17} \text{ m} \left(\frac{P_{abs}}{1 \text{ W}} \right) \left(\frac{500 \text{ Hz}}{f} \right)^2 RIN \quad (3.1)$$

And the strain noise:

$$\delta h_{RP}(f) = \frac{2\delta l(f)}{1200 \text{ m}} \approx 6.1 \cdot 10^{-27} \left(\frac{P_{abs}}{1 \text{ W}} \right) \left(\frac{500 \text{ Hz}}{f} \right)^2 \left(\frac{RIN}{10^{-7} \frac{1}{\sqrt{\text{Hz}}}} \right) \quad (3.2)$$

with the average absorbed power of the CO₂ laser $\langle P_{abs} \rangle$, the speed of light c and the mass m of the beam splitter. Now we can calculate the needed RIN -value, considering that the strain sensitivity should be better than one tenth of the GEO-HF target sensitivity, therefore we get from the radiation pressure (with $P_{abs} = 7.5 \text{ W}$ for GEO-HF):

$$\begin{aligned} \delta h(100 \text{ Hz}) < 10^{-23} & \Rightarrow RIN < 8.7 \cdot 10^{-7} / \sqrt{\text{Hz}} \\ \delta h(500 \text{ Hz}) < 10^{-24} & \Rightarrow RIN < 2.1 \cdot 10^{-6} / \sqrt{\text{Hz}} \\ \delta h(1000 \text{ Hz}) < 2 \cdot 10^{-24} & \Rightarrow RIN < 1.7 \cdot 10^{-5} / \sqrt{\text{Hz}} \end{aligned}$$

This seems manageable. Since it falls quadratically with the frequency, the radiation pressure noise does not pose a problem. The other and for high frequencies more important contribution comes from thermal noises, which only fall linearly with the frequency. We can set up a limit for the thermal noise. For an upper limit we can consider a heating beam which has the same beam profile as the signal beam. Following [Bal06], there are three effects of thermal noise:

1. Expansion of the optic

$$\delta l_{exp} \approx \frac{RIN}{f} \frac{P_{abs}}{2\pi C\rho} \frac{1}{\pi w^2} (1+\eta)\alpha \approx 4 \cdot 10^{-20} \text{ m} \left(\frac{P_{abs}}{1 \text{ W}} \right) \left(\frac{500 \text{ Hz}}{f} \right) \left(\frac{RIN}{10^{-7} \frac{1}{\sqrt{\text{Hz}}}} \right) \quad (3.3)$$

2. Change of the refractive index

$$\delta l_{ref} \approx \frac{RIN}{f} \frac{P_{abs}}{2\pi C\rho} \frac{1}{\pi w^2} \left[(n-1)(1+\eta)\alpha + \frac{dn}{dT} \right] \quad (3.4)$$

$$\approx 5.8 \cdot 10^{-19} \text{ m} \left(\frac{P_{abs}}{1 \text{ W}} \right) \left(\frac{500 \text{ Hz}}{f} \right) \left(\frac{RIN}{10^{-7} \frac{1}{\sqrt{\text{Hz}}}} \right) \quad (3.5)$$

3. Flexing of the optic

$$\delta l_{flex} \approx \frac{RIN}{f} \frac{P_{abs}}{2\pi C\rho} \frac{6\alpha}{D^2} C_{num} \approx 10^{-20} \text{ m} \left(\frac{P_{abs}}{1 \text{ W}} \right) \left(\frac{500 \text{ Hz}}{f} \right) \left(\frac{RIN}{10^{-7} \frac{1}{\sqrt{\text{Hz}}}} \right) \quad (3.6)$$

Adding all the noise terms, we get:

$$\delta l_{alltherm}(f) \approx 6.3 \cdot 10^{-19} \text{ m} \left(\frac{P_{abs}}{1 \text{ W}} \right) \left(\frac{500 \text{ Hz}}{f} \right) \left(\frac{RIN}{10^{-7} \frac{1}{\sqrt{\text{Hz}}}} \right) \quad (3.7)$$

Thus we would get a strain sensitivity $\delta h_{alltherm}$ of

$$\delta h_{alltherm}(f) = \frac{2\delta x_{alltherm}}{1200 \text{ m}} = 1.1 \cdot 10^{-21} \left(\frac{P_{abs}}{1 \text{ W}} \right) \left(\frac{500 \text{ Hz}}{f} \right) \left(\frac{RIN}{10^{-7} \frac{1}{\sqrt{\text{Hz}}}} \right) \quad (3.8)$$

With an assumed RIN of 10^{-7} and $P_{abs} = 7.5 \text{ W}$:

$$\delta h_{alltherm}(100 \text{ Hz}) = 3.9 \cdot 10^{-20} \frac{1}{\sqrt{\text{Hz}}} \quad (3.9)$$

$$\delta h_{alltherm}(500 \text{ Hz}) = 7.8 \cdot 10^{-21} \frac{1}{\sqrt{\text{Hz}}} \quad (3.10)$$

$$\delta h_{alltherm}(1000 \text{ Hz}) = 3.9 \cdot 10^{-21} \frac{1}{\sqrt{\text{Hz}}} \quad (3.11)$$

Most of the values used above are given in appendix A.6 on page 78. $D = 8 \text{ cm}$ is the thickness of the BS. The numerical coefficient C_{num} , that describes the overlap between the CO_2 - and the Nd:YAG laser beams for the flexing noise was arbitrarily chosen to be $C_{num} \approx 1$. This factor will have no influence on the end result, as it is only used for the flexing noise, which is completely dominated by the noise in the refractive index noise.

We can see that the use of a CO_2 laser with a RIN of 10^{-7} yields a high upper limit for the induced thermal noises. The results are visualized in fig. 3.1. Since it is even above GEO's current sensitivity, this is not an option for a thermal compensation in the beam splitter.

3.2.2 Noise caused by a Thermal Radiation based Compensation System

While a CO_2 laser produces coherent radiation, a thermal heat source, sometimes called black body, produces incoherent radiation. As already pointed out by Lawrence in [Law03], a black body thermal correction system features a much lower relative intensity noise, since the emission of the photons is uncorrelated. The RIN is found to be

$$RIN = \frac{\Delta P}{P} = \sqrt{\frac{8k_B T}{P}} \approx 1.4 \cdot 10^{-10} \frac{1}{\sqrt{\text{Hz}}}. \quad (3.12)$$

Which is a factor of 500 less than a very well stabilized CO_2 laser. Here k_B is the Boltzmann constant, $T \approx 1300 \text{ K}$ the temperature of the heater and $P_{abs} \approx 7.5 \text{ W}$ the absorbed heating

power. Using these numbers with equations 3.2 and 3.8, we get:

$$\delta h_{RP}(500 \text{ Hz}) = 6.4 \cdot 10^{-29} \frac{1}{\sqrt{\text{Hz}}} \quad (3.13)$$

$$\delta h_{alltherm}(500 \text{ Hz}) = 1.2 \cdot 10^{-23} \frac{1}{\sqrt{\text{Hz}}} \quad (3.14)$$

It shows that a thermal radiation based compensation system would induce much less noise in the beam splitter than a CO₂ laser based one. In fact the induced noise is about 10 times smaller than the design sensitivity of GEO-HF at 1 kHz.

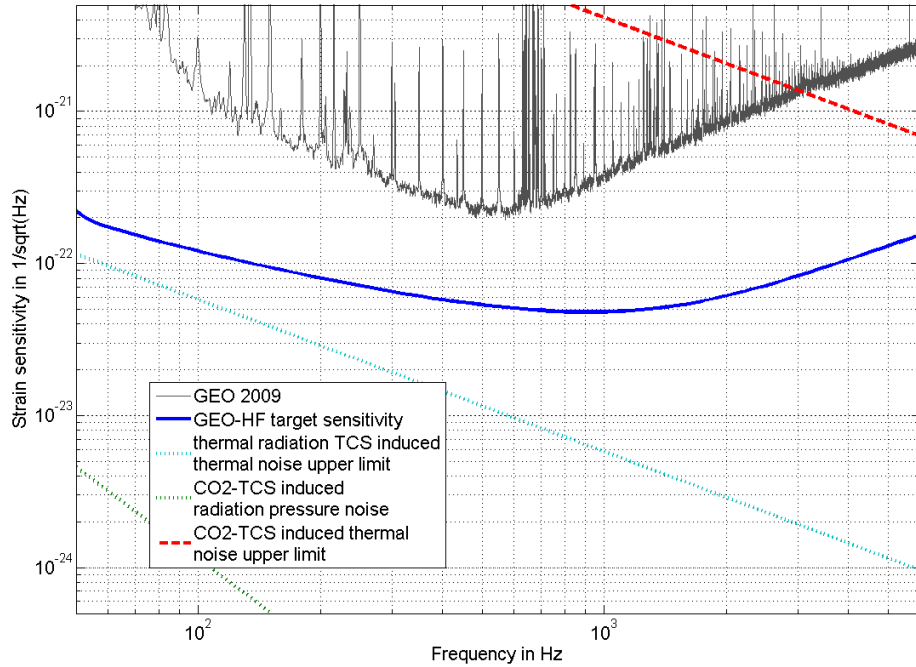


Figure 3.1: This image shows the current GEO 600 sensitivity and the noise that would be caused by a CO₂ based thermal compensation system with an assumed RIN of 10⁻⁷. For the additional photothermal noise, the upper limit is plotted. The radiation pressure noise that would be caused by a thermal radiation based TCS is too small to be included in this plot.

Chapter 4

Simulations

4.1 Introduction

In this chapter I want to present the procedure of simulating the thermal lensing and the thermal compensation system. The tools used for the simulations were Matlab¹, ANSYS², FRED³ and FINESSE⁴ ([FHL⁺04]). FRED is a raytracing program, which was used for the design of the compensation system.

The foundations of the computer model used in this thesis were laid by Tilo Sperling and Jérôme Degallaix in [Spe08].

4.1.1 The Computer Model

For the simulations, a finite elements model (**FEM**) of the BS was created with the aid of the software ANSYS 11. Finite element modeling is a widespread approach to numerically solve mechanical and thermal problems. First, the object to be analyzed is divided into a large number of tetraeders or quaders, defined by their edge points, often called nodes. The boundary conditions are applied to the nodes and equations describing the physical properties for each node. Thus these conditions are set up in a system of equations. These equations are then solved numerically to derive the desired physical properties at each node. In this thesis, a model with 175000 nodes was used to calculate the temperature distribution and the mechanical deformation of the beam splitter. The elements of the FEM can be seen in fig. 4.1. One important aspect of a FEM is the size of the elements. If they are too big, the results will not

¹<http://www.mathworks.com>

²<http://www.ansys.com>

³<http://www.photonengr.com>

⁴<http://www.rzg.mpg.de/adf/>

be very accurate, while too small elements waste computational time. The characteristic length of the thermal lensing problem in GEO 600 is the laser beam waist size $w_y = 1$ cm. The finite elements near the optical path should be smaller than w_y . To speed up the computation, the

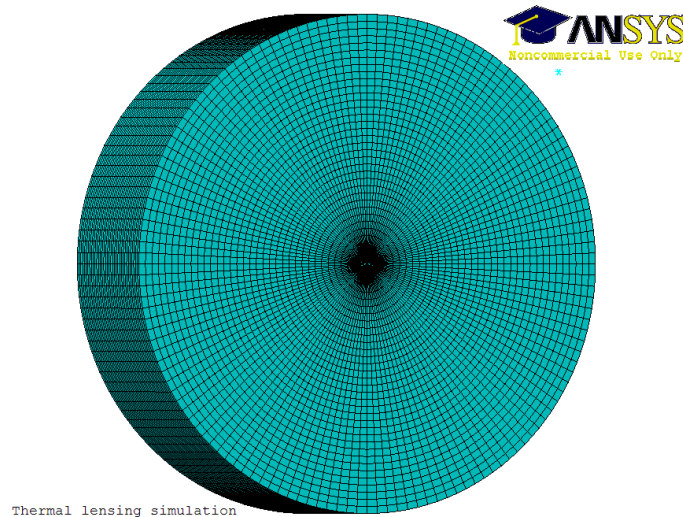


Figure 4.1: Finite elements model of the beam splitter. The elements are smaller in the central region of the beam splitter

following simplifications were made:

- The temperature in the BS causes a deformation, but the effect of the deformation on the temperature was neglected. Instead of a fully dynamical simulation of the mechanical and thermal properties of the BS, first a thermal and then a mechanical simulation were done. Considering the minuscule size of the deformation, it is a reasonably good approximation. Comparisons with fully dynamical interactions have been done too, showing that both ways practically yield the same results.
- While the mechanical stress is included in the finite element model, its influence on the optical path length in the beam splitter is very small in comparison to the thermo refractive effect, as already pointed out in section 2.1.5. It was not included in the simulations.

The work flow for finding the right heating pattern is pictured in 4.2. First the absorption for the laser and a possible TCS is calculated for each point of the BS using Matlab. Then this data is imported into ANSYS which computes the heat distribution and the deformation of the BS. The output is imported into Matlab again to calculate the scattering loss to characterize the performance of the thermal compensation. The scattering loss is explained in more detail in the

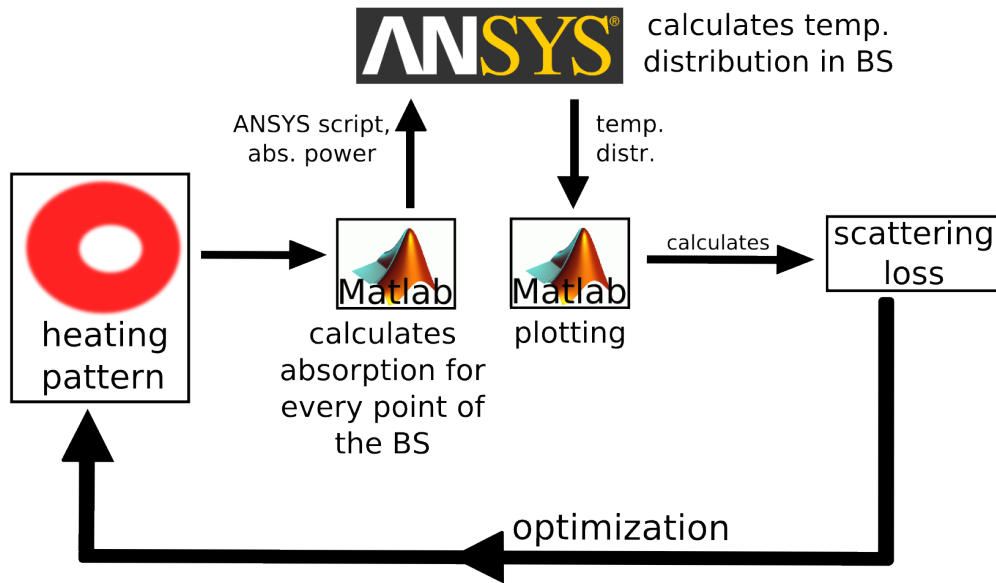


Figure 4.2: Work flow for the simulation

next section. The effect that the thermal compensation would have on the interferometer as a whole was computed using the interferometer simulation software FINESSE. For this purpose, phasemaps for the BS would be generated by the FEM and then be read into FINESSE.

4.2 Scattering Loss as a Measure of Thermal Lensing

The simple thermal lensing model in 2.1.1 uses a parabolic fit of the optical path difference (OPD) to approximate the focal length of the thermal lens. Although very intuitive, this is not always a good way to characterize the thermal lensing. Especially if the OPD is further distorted by a thermal compensation system (TCS), a parabolic fit might not always be suited to the characterize the thermal lens. Because of that it is necessary to introduce another measure of the thermal lensing for the simulations: the scattering loss. Thermal lensing decreases both the contrast at the output and the circulating laser power. This happens because the thermal lens causes scattering into higher order modes, which are not resonant and therefore exit the interferometer at the darkport. First, the optical path difference is calculated for every path parallel to the optical axis. The paths can be described by the coordinates (x, y) at which they enter the BS. It follows: $OPD(x, y) = [Temp(x, y) - 300K] * \beta * L$. Here $OPD(x, y)$ denotes

the optical path delay for all paths parallel to the optical axis, which enter the BS surface at the point (x,y) . $Temp(x,y)$ is the average temperature in the BS for each of this paths, β is the thermo refractive coefficient for fused silica, and L is the length of the optical axis in the BS.

The fraction of scattered power can then be quantified: the overlap between the incoming laser field and the laser field with the OPD applied is calculated, then the scattering loss can be calculated as ([Hel01]):

$$\Theta_{SL} = 1 - \left| \int_0^\infty \Psi_{00}(x,y) e^{\frac{-2i\pi OPD(x,y)}{\lambda}} \Psi_{00}(x,y) \right|^2. \quad (4.1)$$

Eq. 4.1 gives the fraction of the scattered light power. $\Psi_{00}(x,y)$ is the normalized amplitude of the laser beam, which is assumed to be a TEM₀₀ beam.

4.3 Thermal Lensing - Situation in GEO 600

At the power level during this work of approximately 2.7 kW in the power recycling cavity, the thermal lensing effect does not limit the sensitivity or the power build up. However, it is observable in the output beam shape, which is different for a hot and a cold interferometer ([HLW⁺06]). The OPD for the thermal lens can be approximated with a parabolic OPD, which would be caused by an ideal thin lens. The fitting of the OPD with a parabola needs to be performed with the weighting of the laser beam intensity. This approach is a good approximation within the beam waist. Fig. 4.3 shows the simulated optical path differences in the x (= horizontal) and y (=vertical) directions in the GEO 600 beam splitter for the current laser power. Also a parabolic fit, as described before, is plotted in this figure. The effective focal lengths in x and y direction are not the same. This becomes clear, when you consider that the beam enters the BS at an angle in the horizontal direction, therefore the beam gets spread out in this direction. The calculation via ABCD matrix method is given as appendix A.2. The plot in fig. 4.3 further shows that the current thermal lens in y-direction can be approximated with an ideal thin lens of a focal length of $f_{therm-sim-y} = 5.84$ km. This agrees within 6 % to the value of $f_{therm-model-y} = 6.2$ km given by the analytical model in formula (2.4), while for the x-direction the beam waist size is larger by a factor of 1.2. This leads to a longer thermal lens: $f_{therm-sim-x} = 8.03$ km. With a waist size of $w_x = 1.2$ cm, formula (2.4) gives $f_{therm-model-x} = 8.8$ km. The agreement of the model and the simulations are still of an acceptable 9%.

Apart from being observable in the output beam shape, the thermal lens does not yet affect the interferometer much. The focal length of the thermal lens is much bigger than the arm

length, and the signal recycling additionally improves the thermal lensing situation, as shown in the next section. But with the planned power increase of a factor eight, the situation looks

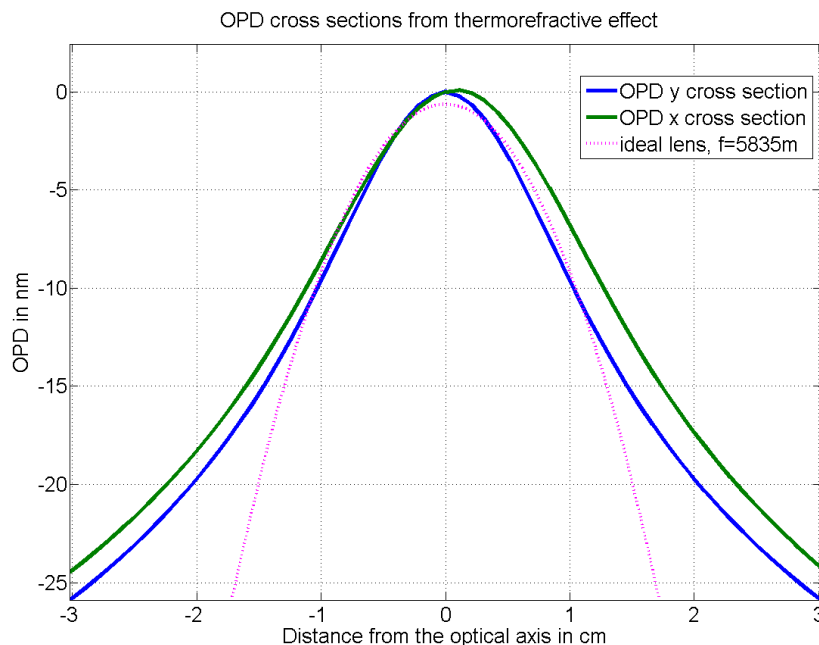


Figure 4.3: Thermal lensing in the beam splitter. The cross sections of the optical path difference after passing the GEO beam splitter are plotted. The optical path difference arises from the thermal lensing effect in the BS, for a laser power of 2.7 kW in the BS. No thermal compensation is assumed. The OPD can be fitted with the OPD caused by an ideal thin lens with a focal length of 5835 m.

different: As equation 2.4 shows, the focal length of the thermal lens changes inversely to the laser power. The focal length f_{therm} would then drop below the optical arm length of 1200 m. It would seriously interfere with the power build up in the interferometer, so that it is likely that this power level will not be reachable without a thermal compensation system. The expected power build up with regard to the thermal lensing is further examined in section 4.5.4.

4.4 Signal Recycling and Thermal Lensing in GEO 600

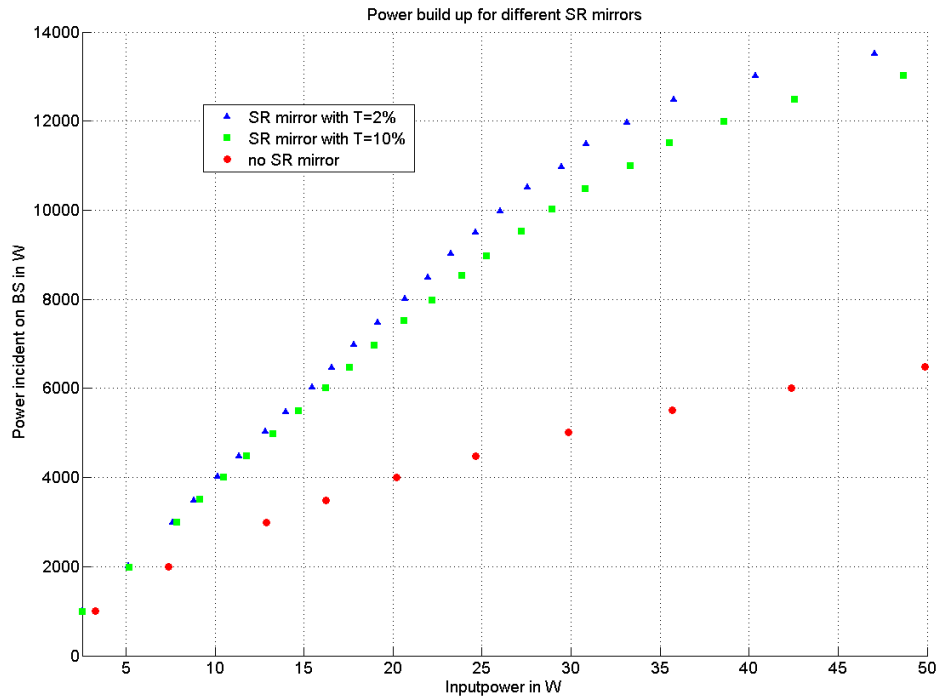
As mentioned in chapter 1.3.1, GEO uses signal recycling. While the main purpose is the amplification of the signal sidebands, it has an impact on the thermal lensing in the beam splitter as well. It is already observed that the power inside the interferometer drops significantly, if the SR mirror is misaligned. The higher power with the properly aligned SR mirror can be explained with the effect of mode healing, like already mentioned in chapter 1.3.1. Given that information, the SR needs to be considered when looking at the intracavity power. A computer simulation,

which compares the effects of different SR mirrors has been done, again using the FEM model and the software FINESSE. The SR mirrors used in the simulations had 2 % transmissivity, like the current one and 10 % transmissivity, like the future one. The case of no signal recycling mirror is also plotted. The results are shown in fig. 4.4(a). For this simulation, all optical parameters, except the SR mirrors are equal. It needs to be noted that the optical configuration of the interferometer in this simulation is the current one. That also means that the scaling of the input power axis would change with the planned installation of new mode cleaner mirrors, because the transmission of the new mode cleaners is planned to be higher than the transmission of the current ones. The only dynamic loss included in this simulation is the thermal lens in the BS. The positive effect of the mode healing on the intracavity power is clearly visible. Even more, with the SR mirrors, the power build up is nearly linear to the input laser power. It shows that with signal recycling, GEO already has a kind of limited thermal compensation, that would work up to intracavity powers of 10 – 12 kW.

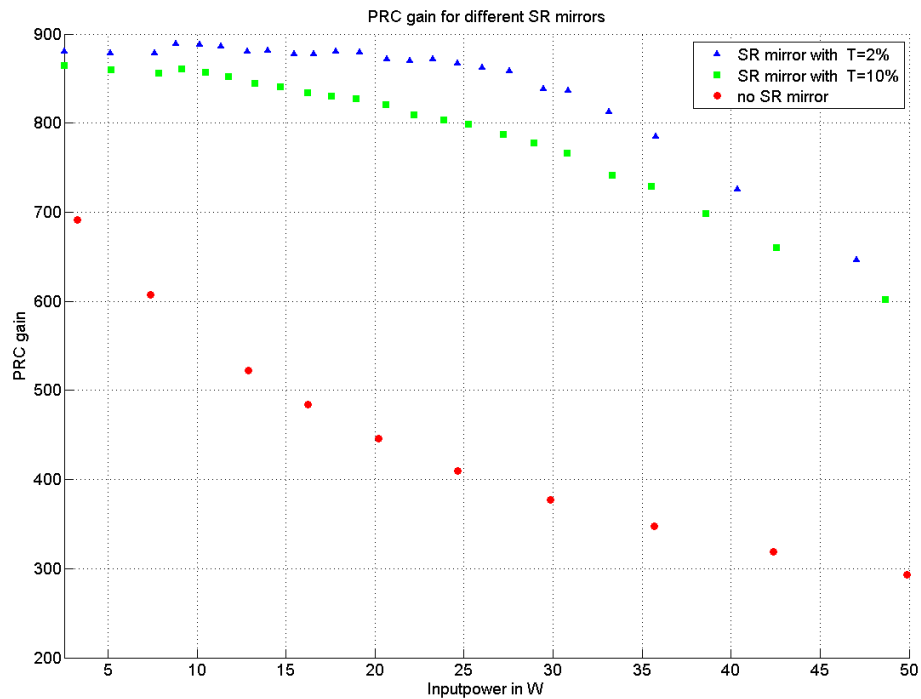
4.4.1 Finding the right Heating Pattern

The heating can be applied to the partly reflective side or the anti reflective coated side of the beam splitter. Also it would be possible to heat both sides of the beam splitter, since viewports exist on both sides of the vacuum tank. The easiest way of compensation would be to apply an annular heating profile on the beam splitter. However this does not lead to optimal results, since the laser beam itself is oval in the BS, as shown in A.2, and it passes the beam splitter at an angle. An optimal heating pattern has to be found. It should be symmetrical in the vertical direction, since the physical situation is symmetrical in this direction. As a result we considered oval ring-shaped patterns. Ten geometry parameters have been chosen to characterize the heating pattern, they are pictured in fig. 4.5. The parameters cover a shift of the inner and outer borders of the pattern in horizontal and vertical direction. Moreover there are parameters describing the extent of the inner “hole” in vertical direction as well as in left and right horizontal direction. Analogue parameters describe the outer border of the pattern. With the selection of those ten geometrical parameters, some possible shapes are already ruled out. However, those ten parameters should offer enough complexity to find a reasonably good compensation pattern.

Finding a good compensation pattern is not trivial. With 11 degrees of freedom, trial and error methods and manual tuning would have taken too long. Especially since evaluating a heating pattern with the FEM-model was an “expensive” computing task. Calculating the scattering loss with a certain compensation pattern took about 30 min on an AMD 2 Ghz Quad core machine. For this reason, a hybrid optimization approach was used: first the pattern was optimized by a genetic algorithm, then the found pattern would be fine-tuned by the Newton method. A general



(a) Power build-up for different SR mirrors - no thermal compensation.



(b) PRC gain factors for different SR mirrors - no thermal compensation.

Figure 4.4: Comparison of signal recycling mirrors with different transmittances.

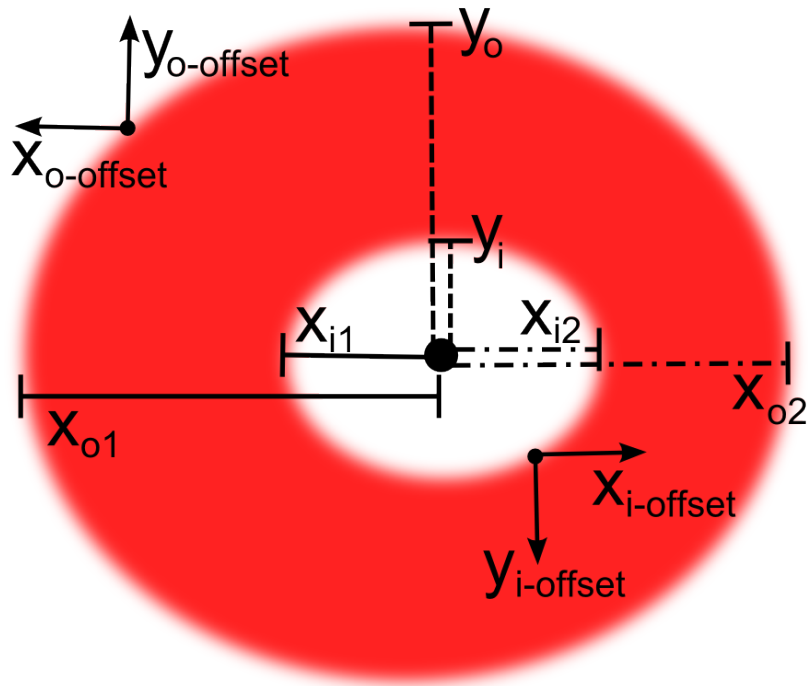


Figure 4.5: Variables of the heating pattern.

The variables with the subscript “offset” denote a shift of the whole inner or outer border of the pattern. The other variables describe the distance of the pattern’s inner and outer border to a central point. “ y_i ” is the distance of the inner border of the heating pattern to the central point. “ x ” and “ y ” denote the horizontal and vertical direction, the subscripts “ i ” and “ o ” specify whether the inner or the outer border of the pattern is meant.

Example: “ y_{i1} ” is the distance of the inner border of the heating pattern to the central point in vertical direction. The 11th variable (not shown here) is the heating power.

description of how a genetic algorithm works can be found in the appendix A.1 or in [Mit98]. The genetic algorithm used a generation size of 20 and converged usually after less than 10 generations, if the parameter range was further restricted. For example, some of the restrictions were that the heating pattern has to be smaller than the BS and that the central hole has to be larger than the laser beam. Genetic algorithms are not guaranteed to find the optimal solution to a problem, but they often find a satisfactory solution quickly.

4.5 Results and Discussion

Several heating patterns that would decrease the scattering loss and increase the focal length of the thermal lens have been found. They vary in size and power, and depending on one's priorities some might be better suited than others. Here I want to present the results for some of the best heating patterns found so far. Their geometry parameters are listed in appendix A.4. The simulations show that good thermal compensation can be accomplished by heating either side of the BS or by heating both sides of the BS. Although the optimal heating patterns would look different in all three situations, they all require similar powers absorbed in the BS for an optimal compensation as measured by the scattering loss.

4.5.1 Scattering Loss and focal Length

The implication for the focal length of the thermal lens is shown in table A.2 for a good narrow heating pattern. "Narrow" refers to the extent of the inner area. Similar tables for a wide pattern, the pattern for the backside heating and both sides heating are supplied in the appendix A.3. Clearly, the compensation system has a positive effect on the focal length of the thermal lens. All of those cases could also reduce the scattering loss significantly. The performance of

	2.7 kw no comp	2.7 kw w comp	20 kw no comp	20 kw w comp
f_x	8031 m	-45066 m	1084 m	26945 m
f_y	5835 m	47592 m	788 m	2359 m
sc. loss	$4 \cdot 10^{-4}$ W	$3.9 \cdot 10^{-5}$ W	$2.4 \cdot 10^{-2}$ W	$2 \cdot 10^{-3}$ W

Table 4.1: Table with values for a narrow pattern.

the compensation system is apparent when looking at the optical path difference in fig. 4.6. It shows cross sections for the OPD in the BS for the narrow heating pattern. A flat OPD profile would be ideal. While the thermal compensation is still not ideally flat, it is a big improvement over the uncompensated OPD profile. There is a sharp drop-off in the OPD profile 2.5 cm away from the optical axis. For GEO this is irrelevant, since the beam waist sizes are only

$w_x = 1.2$ cm and $w_y = 1$ cm. It is important to stress that the compensation gets more difficult

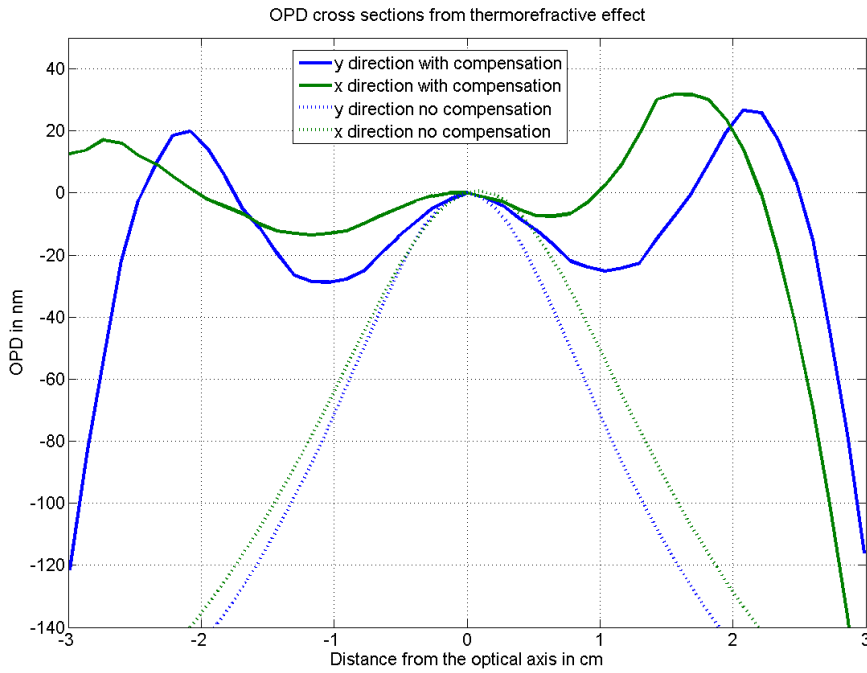


Figure 4.6: Optical path difference cross sections in x (horizontal) and y (vertical) direction for the compensated (narrow pattern) and uncompensated case of a 20 kW laser beam.

with increasing laser power. This means that for a higher power laser beam, the lowest achieved scattering loss is larger than for a laser beam with less power. This can also be seen in fig. 4.7. Another observation is that the optimal compensation power scales linearly with the circulating power. In the case of 20 kW laser power with thermal compensation, the thermal focal length and the scattering loss are worse than for the case of 2.7 kW laser power without compensation.

4.5.2 Temperatures in the BS

The expected temperatures of the BS are plotted as a cross section in the horizontal plane in fig. 4.8. Fig. 4.8(a) shows the temperature for a narrow heating pattern, 4.8(b) for a wide one, and 4.8(c) for the heating from both sides. While the maximal and minimal temperatures of the BS are similar for the first two cases, the heating from both sides features lower maximal and minimal temperatures in the BS for the same amount of power absorbed in the BS.

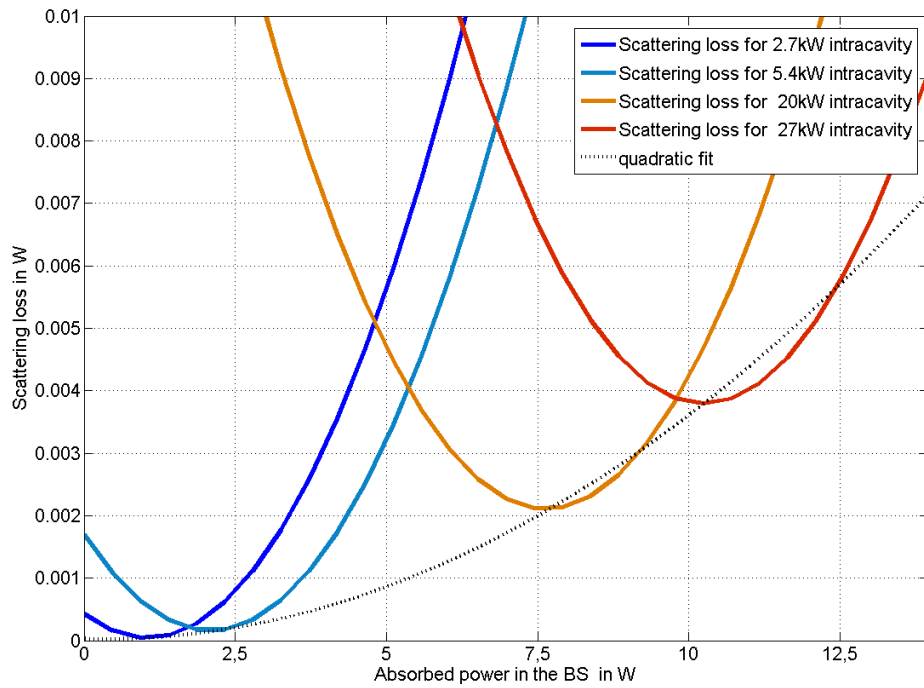


Figure 4.7: Scattering loss in dependence of the power of the thermal compensation system for the narrow pattern.

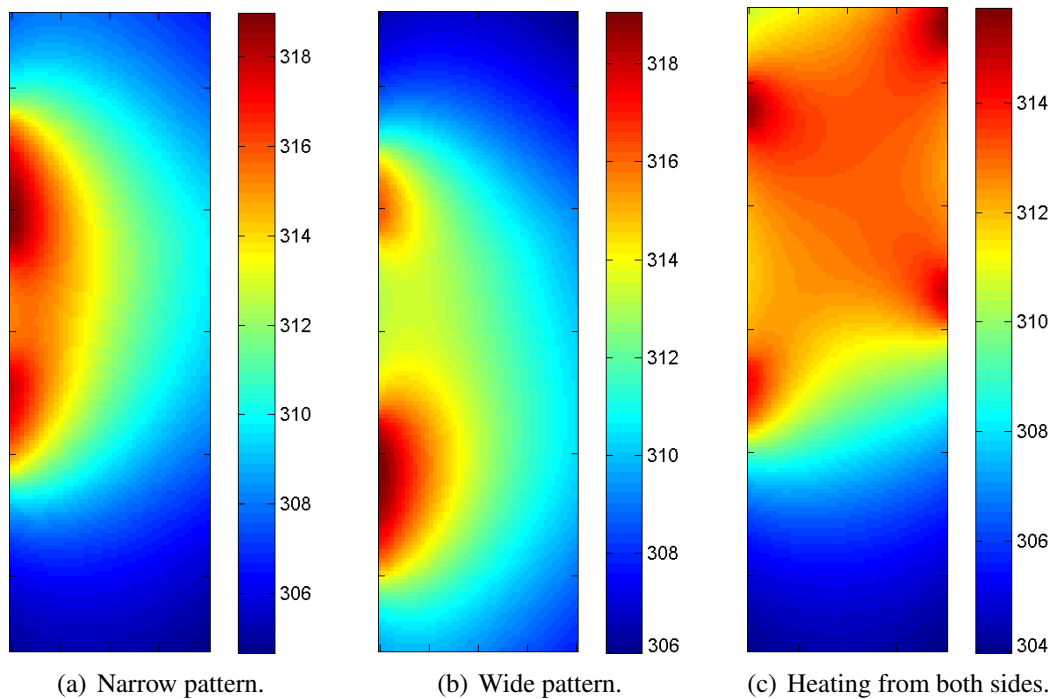
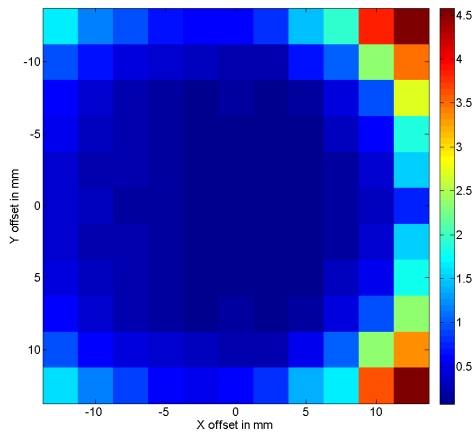


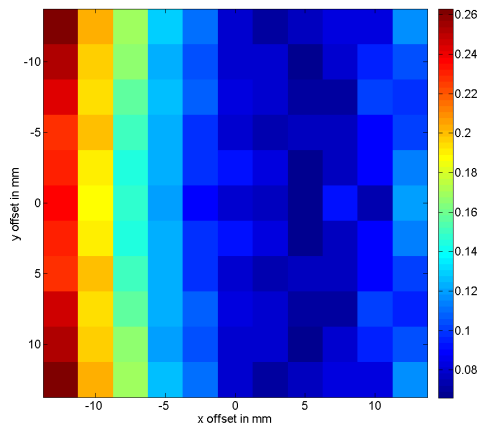
Figure 4.8: Temperature distribution for different heating patterns in the BS. The temperatures are color coded and show the temperature in K, an ambient temperature of 300 K is assumed.

4.5.3 Misalignment of the Heating Pattern

Of course, the TCS is sensitive to misalignment, meaning that the performance of the compensation is affected by the position of the heating pattern on the BS. The sensitivity to misalignment depends on the used heating pattern. Wide patterns are found to be less affected by a misaligned heating of the BS, but require slightly more power for a similar level of compensation. The FEM simulations have been used to determine how good the compensation for a misaligned pattern is. Fig 4.9(a) and 4.9(b) show the performance of the TCS when the whole heating pattern is not centered on the optical axis. The performance of the TCS is color-coded by the scattering loss produced, and has been normalized to the scattering loss without compensation. Therefore, a value of '1' means a scattering loss equal to the situation without a thermal compensation, values smaller than 1 are an improvement. A pattern with a wide free inner region is less affected by misalignment than a narrow one. It can be seen that for the narrow pattern a misalignment of only 0.5 cm is tolerable, while more than 1 cm makes the thermal lensing situation worse. While a wide pattern is much more forgiving, with more than 1 cm shifted, the compensation is still good.



(a) Pattern fig 5.6(c) and 5.6(d)



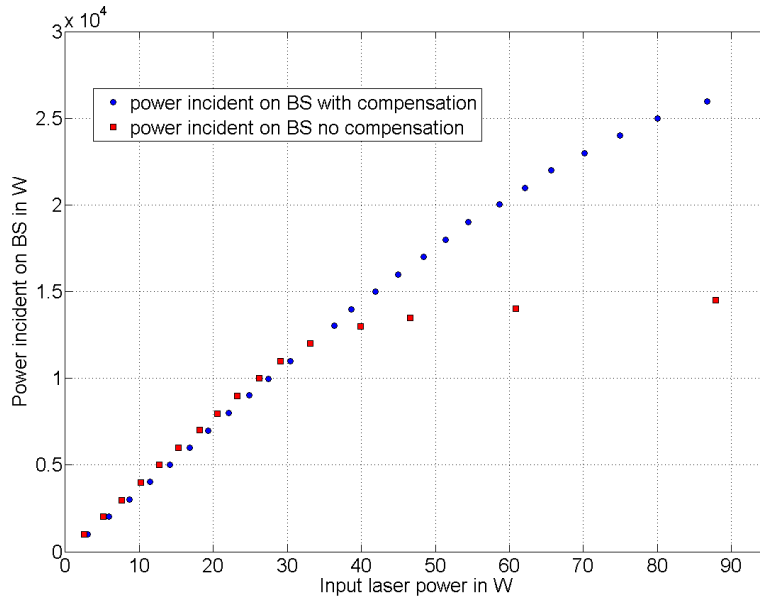
(b) For a wide pattern, shown in fig 5.8(b)

Figure 4.9: Performance for 2 different misaligned heating patterns. The whole pattern is shifted, the colors represent the fraction of scattering loss compared to the case without TCS. The best value reached is 0.07 times the uncompensated scattering loss (for both cases). Please note the different color-scaling of the images.

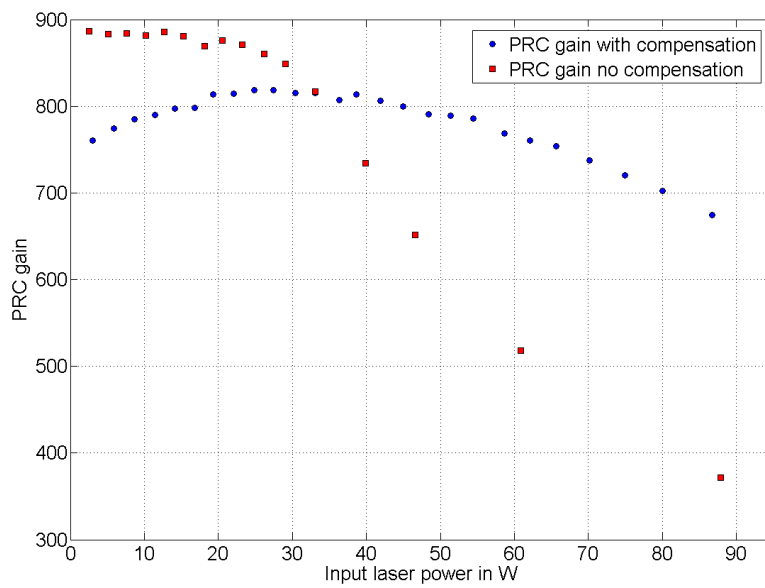
4.5.4 Impact on the Interferometer

In the end, the benefit of a thermal compensation is not measured by the focal length of the thermal lens or the scattering loss, but rather by the power build up in the power recycling cavity and the power at the darkport. Fig. 4.10 and 4.11 show how the compensation would affect the whole interferometer in a FINESSE simulation. A static compensation with 7.5 W absorbed power in the BS and the parameters for today's GEO configuration are assumed. That means that among other things, the changes of the input mode cleaners are not included. With GEO-HF completed, a higher percentage of the input laser power would be injected into the power recycling cavity. Clearly for about 12 kW of circulating laser power and above, the benefits of the compensation show. From there on, the circulating laser power is greater, so the optical gain is higher and the light leaking at the darkport is reduced for the case with compensation. The compensation gives an improvement over a wide range of circulating laser power. Moreover, fig. 4.10(a) indicates that a thermal compensation system is necessary to reach the planned circulating power of 20 kW.

Furthermore it is visible that there is one input power (and therefore laser power inside the interferometer), for which the compensation works best. It is at the point where the optical gain has its maximum, like seen in fig. 4.10(b). The minimum in fig. 4.11(b) for the power leaking out of the darkport per circulating laser power also indicates an optimal heating output for that laser power.

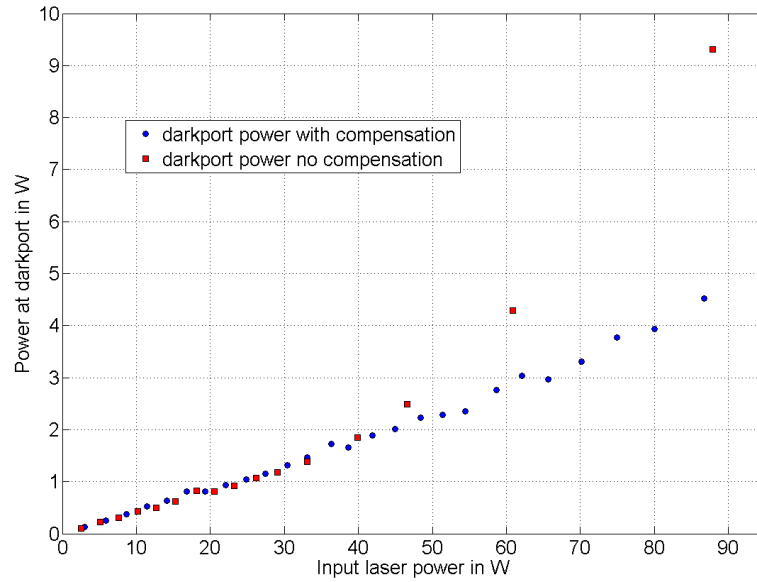


(a) PRC power comparison.

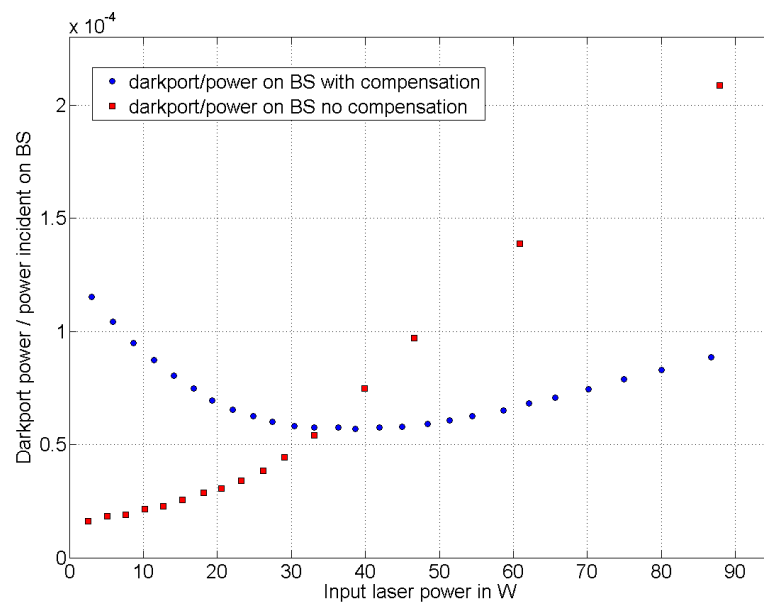


(b) PRC gain comparison.

Figure 4.10: Comparison of circulating power and the PRC gain of GEO with and without a static thermal compensation (narrow pattern).



(a) Power at the darkport.



(b) Ratios of darkportpower/PRCpower.

Figure 4.11: Comparison of the darkport power and the ratio of darkport power to circulating power in GEO with and without thermal compensation.

Chapter 5

Prototype TCS

Using the simulations in the last chapter it was possible to build a test thermal compensation system. This chapter highlights the design requirements, shows the setup and components of the compensation system and features a test of the system.

5.1 Requirements

For designing the thermal compensation system, several constraints and requirements have to be taken into account. Thus, the TCS must

- **be placed completely outside the vacuum system,**
because of space constraints in the vacuum tank. This way, there is also no risk of the TCS blocking the laser, or one of the several pickup beams coming from the BS.
- **scale with the power upgrade.**
It needs to be able to compensate for a wide range circulating laser power. Ideally future power upgrades after the planned one would also be covered.
- **produce a tunable heating pattern.**
Since the simulated pattern is asymmetric, and different patterns are required for AR-, BS and both sides heating, an adjustable shape of the heating pattern is desirable for the TCS.
- **be suited for permanent use.**
For science runs it is essential to have the TCS running permanently.

- **not add too much noise.**

Of course the compensation system should not limit the sensitivity of the interferometer.

5.2 Setup

To meet the requirements mentioned above, it was decided to set up a TCS, which emits radiation in the infrared range to the BS. Since it needs to be outside of the vacuum tank, the radiation must pass through a viewport. Fortunately, viewports facing both the AR and the BS-coated sides are available, and could be replaced by broadband-AR-coated zinc-selenide (**ZnSe**) viewports of 100 mm diameter. ZnSe has a high internal transmission for a wide range of infrared radiation from $0.6 \mu\text{m}$ to $16 \mu\text{m}$ ([SS84]). For ease of use and the noise considerations explained in chapter 3.2.1, the source of the radiation was chosen to be a black body.

The setup consists of 2 polished aluminum parabolic mirrors facing each other and sharing a common focal point. The mirrors have to be large because of the extended source. The thermal source is located in the focus point. It is a heating wire, wound up to a coil. The arrangement of the two mirrors and the heating source produces an annular beam of infrared radiation. To make it pass through the smaller viewport and project it on the BS, an IR-Fresnel lens was used. The setup is pictured schematically in fig. 5.1, while fig. 5.2 shows a photo of the prototype system and a dummy beam splitter.

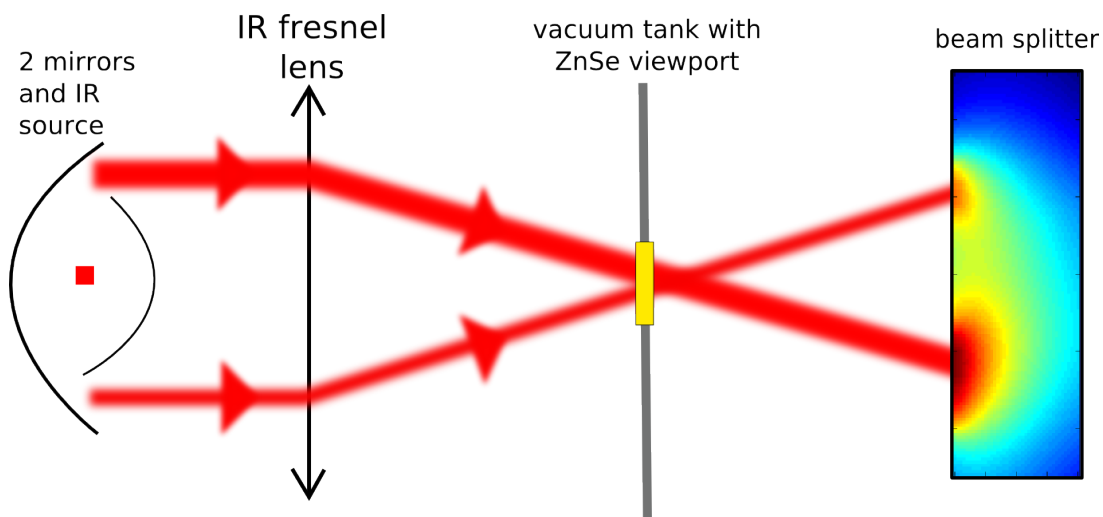


Figure 5.1: Schematic setup of the TCS prototype system, viewed from above.

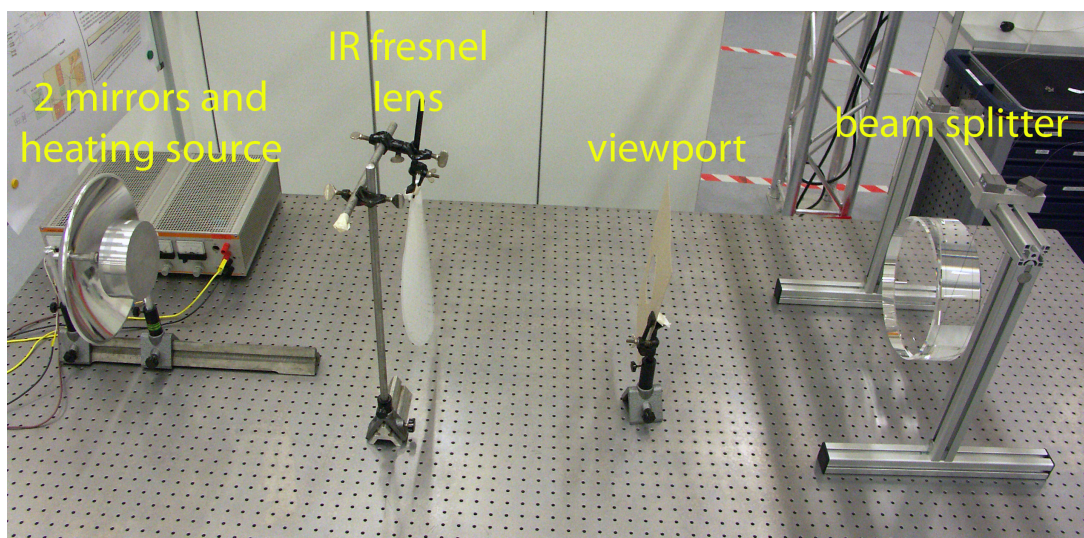


Figure 5.2: Photo of the actual TCS prototype system.

5.2.1 Components

The test system consists of 2 parabolic aluminum mirrors, an IR Fresnel lens and an IR source. The smaller mirror was made in our workshop, has a focal length of 3 cm and a diameter of 13 cm. The bigger mirror was obtained from Edmund Optics¹ has a diameter of 30.4 cm and a focal length of 7.6 cm. For a classical spotlight configuration the smaller mirror would be a spherical one, this would also allow a higher output power. Simulations in FRED however showed that a spherical mirror would somewhat degrade the shape of the heating pattern. Because of that and because the output power should be sufficient (see section 5.2.3), it was decided to use a parabolic mirror. It would reflect the radiation back to the filament heating it up even more and increase the output in that way.

5.2.2 The IR Fresnel Lens

Three different IR Fresnel lenses were used for the prototype TCS. They were ordered from the company OASYS, and are made from the proprietary material² “Poly IR 2”. They have a diameter of 305 mm and focal lengths of 411 mm, 440 mm and 520 mm in the infrared range. Having a low dispersion, the focal lengths can be treated as constant in the range from visible light to 10 μm . They are opaque in the visible wavelength range. According to the data sheet, the lenses have a varying transmission, that can be averaged to be 50% in the range from 3 – 12 μm . A transmission spectrum is included as appendix A.5. This type of lens has been selected

¹<http://www.edmundoptics.com>

²More information on this material can be found on <http://www.fresneltech.com/>

for cost reasons, a zinc-selenide or germanium lens of this size would have been prohibitively expensive.

5.2.3 The Heating Source

The IR source is made from Kanthal D wire. Kanthal is usually used for heating applications. The maximum continuous operating temperature in air is specified to be 1600 K. It has a high specific resistance, making it an efficient heating source. The temperature dependency of the resistance is also relatively low, at 1300 K the resistance is 7% higher than at room temperature (data taken from [All97]). With a diameter of $d = 0.4\text{ mm}$ the resistance for this wire is



Figure 5.3: Photograph of the heating wire with the more efficient winding, as mentioned in section 5.3.2.

$10.7\ \Omega/\text{m}$ (manufacturer data). Kanthal contains aluminum and when heated up in air, it forms an outer layer of aluminum oxide. For the purposes of this thesis, this property is very useful in insulating the windings of the heating wire from each other. The wire used for the heating system had a length of $l = 30\text{ cm}$, therefore a resistance of $3.2\ \Omega$ and an area of $\pi \cdot d \cdot l \approx 0.0038\text{ m}^2$.

Power of the Thermal Compensation System

This section gives a calculation of the power of the thermal compensation system. The emitted power of radiation scales with the fourth power of the temperature, while convection and heat conduction scale linearly with the temperature difference. At temperatures in the range of $1000\text{ }^\circ\text{C}$, emission of radiation is the dominant way of energy transfer, and assumed to be the only one. Now there are several sources of loss to consider. Since the heating coil is placed

between two mirrors, only the radiation that is emitted into a certain solid angle can leave the system of the two mirrors. The other part of the radiation is reflected back onto the other mirror and finally to the heating source, heating it up more. With the mirror focal lengths and diameters, some geometry leads to an “acceptance angle” of approx. 3 sr, hence one quarter of the radiation is transferred to the lens. There is a loss at the reflection of the mirror too. This loss is assumed to be in the order of 15 %. Made out of plastic, the IR Fresnel lens is not completely transmissive for infrared radiation. The lens has a transmission of approximately 50 %. Furthermore, the beam splitter does not absorb all of the radiation. Only the absorbed power fraction by the beam splitter substrate is relevant for heating the BS. The BS shows significant absorption only for only wavelengths longer than 2.5 μm , as shown in fig. 5.4. With the absorption spectrum, the power fraction in the relevant wavelength range can be computed for different temperatures of the heating source. This has been done numerically. For the radiation of a 1300 K source, about 66 % of the power is absorbed by the beamsplitter. Putting everything together, a thermal compensation system with an electrical power of $P_{in} = 100 \text{ W}$ with a 1300 K hot heating source has a potentially useful output of

$$P_{out} = P_{in} \cdot \frac{1}{4} \cdot 0.85 \cdot 0.5 \cdot 0.66 \approx 11.5 \text{ W} \quad (5.1)$$

in the wavelength range from 2.5 μm to 16 μm .

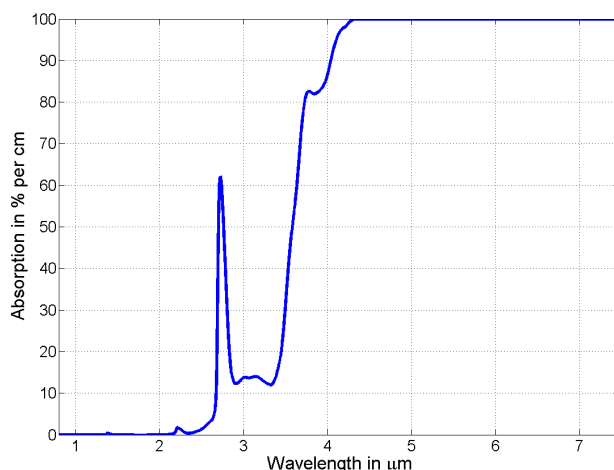


Figure 5.4: Absorption spectrum of fused silica.

Measuring the Temperature of the Heating Wire

The temperature measurement of the heating wire was done using a type K thermocouple and a multimeter (METEX M-3660D). With this kind of measurement the temperature has a tendency to be underestimated, because of a non-optimal coupling of the thermocouple and the heating wire. Another method of measuring the temperature using the electrical resistivity of the wire failed. Most likely the forming oxide layer has an effect on the resistivity that cannot be neglected. With the area of the wire, the electrical power and the emissivity $\epsilon = 0.7$, the temperature reached by the heating spiral could be calculated using the Stefan-Boltzmann law. However, the calculated temperatures are around 300 K less than the measured ones by the thermocouple. The Stefan-Boltzmann law does not apply, because it assumes that the radiation leaves the hot object. But in this case it is wound up and therefore the radiation (and to a smaller part convection) from one part of the spiral heats up another part of the spiral.

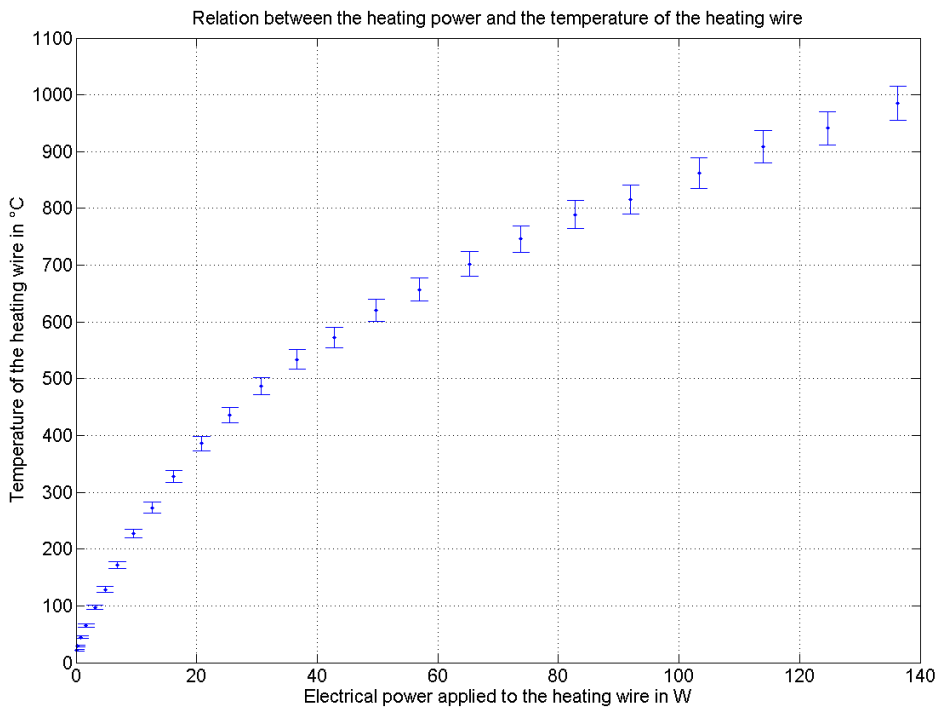


Figure 5.5: Temperature of the heating wire for different electrical powers.

A 50 W halogen lamp was used for the alignment of the system. The visible throughput from the IR Fresnel lens was sufficient for this. For the testing of the system, the heating pattern was projected on a piece of cardboard.

5.2.4 Alignment and Shaping of the Heating Pattern

With all the optical elements centered, the TCS produces an annular heating pattern. Since the desired pattern is asymmetric in the horizontal direction, some adjustments of the optical setup have to be made. An half-elliptical mask can be employed between mirrors and lens to clip inner parts of the annular beam. This way the inner “free” part gets the double elliptical shape that was simulated. The big and small mirror can be turned in the horizontal plane. This assures the elliptical outer shape of the heating pattern. The size of the pattern can be influenced by choosing lenses with different focal lengths. The distance between lens and viewport/BS cannot be varied much. It needs to be considered that the viewport should not clip the heating beam.

5.3 Results and Discussion

5.3.1 Reproducing the simulated Heating Patterns

The achieved heating patterns need to be compared to the simulated ones. For this, the heating wire was heated up to a point that the heating pattern became visible. A photograph of the pattern was taken. Fig. 5.6 presents achieved light distributions and the simulated patterns as lines. The optimal simulated patterns found by the simulations can be created with the TCS setup. Central heating is also possible, illustrated by fig. 5.7. This would allow a faster recovery to a thermal steady state if the lock has been lost.

5.3.2 IR Pictures and Power of the TCS

To complement the measurements in the visible range, IR pictures of the BS have been taken, to show its temperature. For this purpose the BS was suspended as a single pendulum to minimize the effect of heat conduction to the ground. The camera used here was a Varioscanner 3021-ST by Jenoptik, it is specified to have a thermal resolution of 0.03 K and produces pictures of 360x240 pixels. Its thermal range covers $-40\text{ }^{\circ}\text{C}$ to $1200\text{ }^{\circ}\text{C}$. The thermography of a nearly steady state temperature distribution in the BS is presented as fig. 5.8(a). Figure 5.9 shows the temperature profile on the heated BS face. As the IR pictures show, the visible output of the heating pattern does transfer directly into a temperature distribution in the BS, but the measured absolute temperatures are far from the simulated ones. One reason is that the BS did not reach thermal equilibrium. Another reason for this may be that the simulations assume vacuum, while the prototype BS was suspended in air. In air we can expect much lower temperatures due to heat conduction to the air and due to convection. In this case, the dominant way of heat transfer

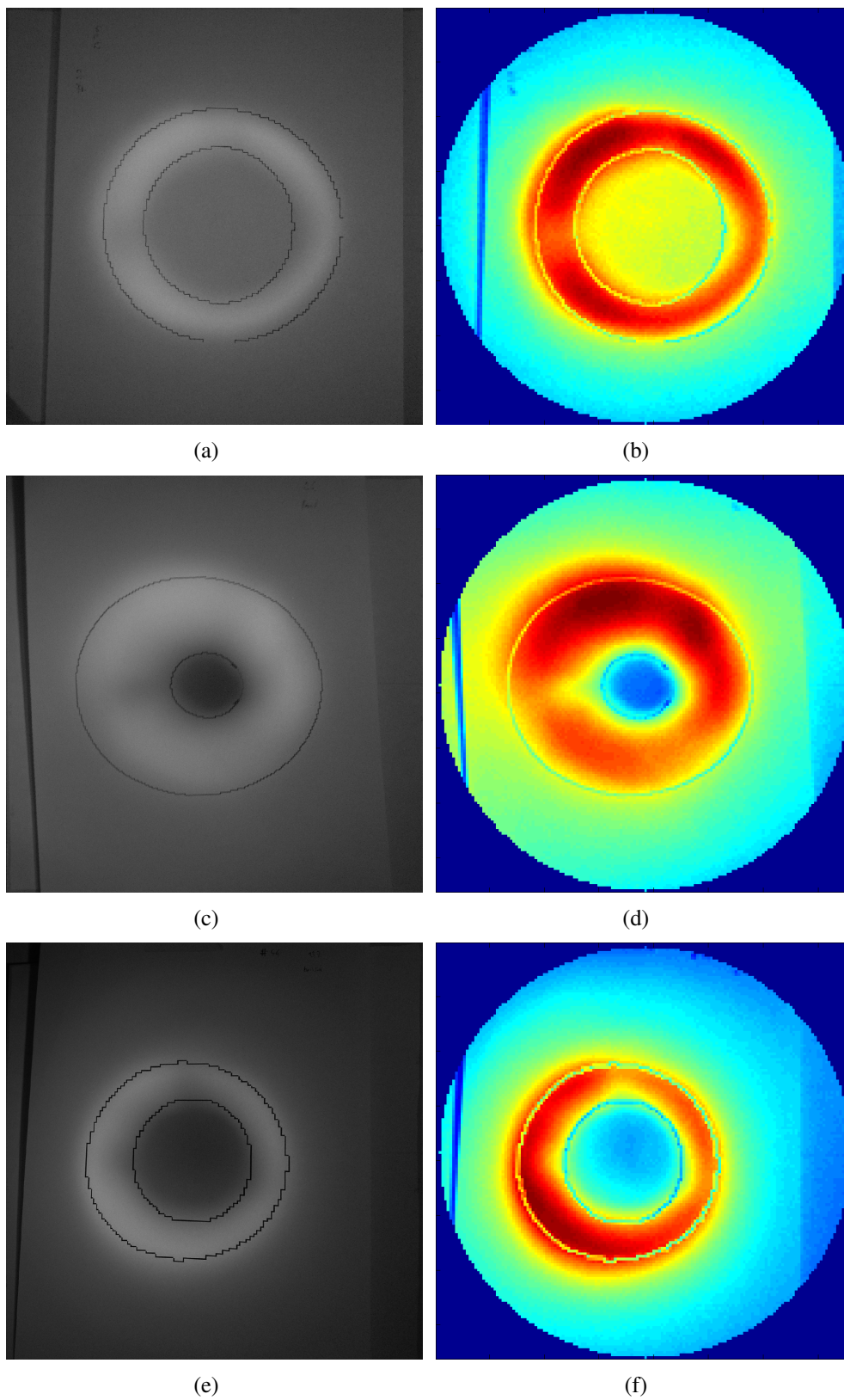


Figure 5.6: Possible heating pattern shapes. Pictures have been taken in the visible range (left), then color-coded to show the intensity distribution (right). Fig. 5.6(e) and 5.6(f) is a pattern suited for heating the AR side of the BS.

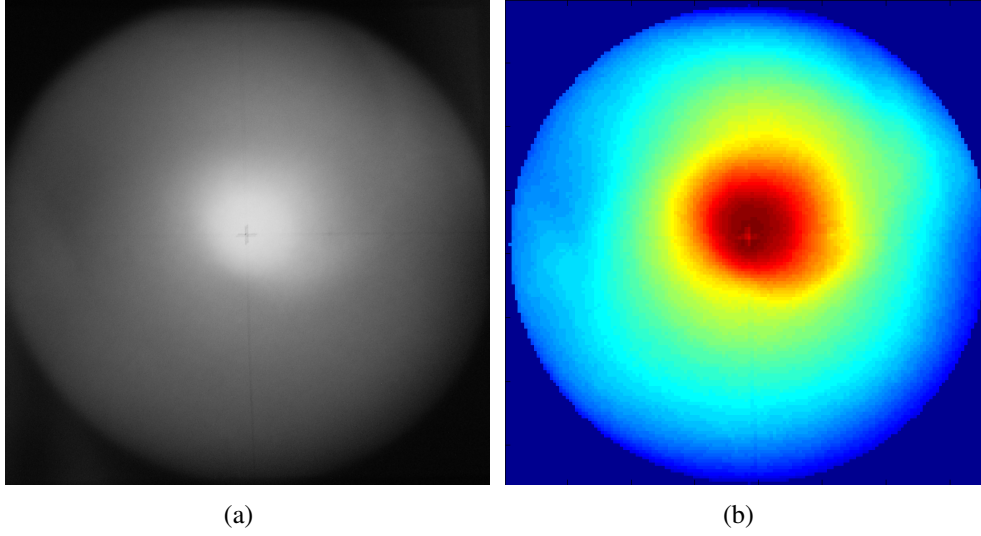


Figure 5.7: Central heating of the BS.

from the BS to the surrounding is convection. The radiative heat transfer can be estimated with the Stefan-Boltzmann law. If we only consider the heated BS face with the area A_{face} and assume a temperature of $T = 24\text{ }^{\circ}\text{C} \hat{=} 297\text{ K}$ (extrapolated from fig. 5.10), the radiated power is:

$$P = \sigma A_{face}(T^4 - T_{room-observed}^4) \approx 0.6\text{ W}. \quad (5.2)$$

A surrounding temperature of $T_{room-observed} = 294\text{ K}$ was measured and used here.

The power loss due to convection can be calculated with the Newton model of cooling. It assumes a heat loss of the BS proportional to the temperature difference ΔT between the BS and the surrounding. It makes use of the heat transfer coefficient h , which heavily depends on the surroundings. The literature gives only estimated values for special cases. We will assume a value of $h = 34\text{ W/m}^2\text{K}$ for the beam splitter. This value can be derived from the observed cooling rate of the beam splitter. The exact procedure for doing this is explained in the next section. The cooling power due to natural convection, on the heated side of the BS is (with $\Delta T = 2\text{ K}$):

$$P = hA_{face}\Delta T \approx 3.7\text{ W} \quad \text{with} \quad (h = 34\text{ W/m}^2\text{K}), \quad (5.3)$$

the convective cooling is clearly the dominant cooling mechanism.

The power output of the TCS can be approximated by using the extrapolated thermal steady state temperature of the heated BS side: cooling power and heating power must be equal at the thermal equilibrium. The sum of radiative and convective cooling yield 4.3 W of power loss due to cooling mechanisms for the thermal steady state, leading to a power output of the TCS of 4.3 W too. This is less than half of the value given by eq. 5.1, and only 60% of the

required power of 7.5 W. Possible explanations are that a significant amount of power from the heating coil is lost due to convection and conduction through the pins that hold it, or that the larger aluminum mirror has a reflectivity worse than the assumed 85 %. The power needs to be increased by at least a factor of two. That should be possible, the preferred change would be new heating filament.

The power of the emitted radiation scales linearly with the radiating surface. Therefore increasing the surface area is one way to increase the radiated power. Through tighter winding it was possible to create a new coil with the same dimensions as the old one, but with an overall wire length of 60 cm. Along with a fitting power supply, it could produce twice as much radiation as the first coil.

Also, higher temperatures of the heating wire would increase the emitted power. Another benefit would be that compared to convection, the emitted power fraction through radiation increases with the temperature of the radiating surface.

If found to be necessary, increasing the power of the TCS can also be done by replacing the smaller mirror by a spherical one. Gold-coating of the mirrors could also improve the output power.

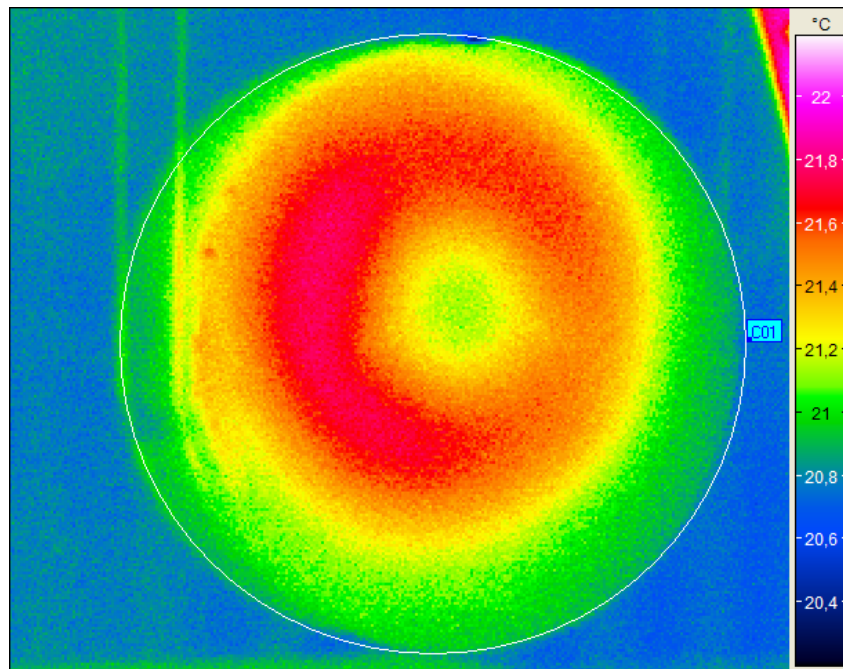
5.3.3 Time Dependence of the Temperature Distribution

The time dependence of the temperature distribution in the BS has also been investigated. As a result, figure 5.10 shows the maximal, minimal and average temperature of the heated side of the BS over time. Simple calculations in chapter 2.3 led to a predicted time constant of about 2 hours for the BS to reach a thermal steady state. This calculation assumed vacuum though, the time constant in air is expected to be much smaller. With the observed time constant in air, it is possible to estimate its effect on temperature in the BS. Unfortunately the measurement was not long enough for the BS to return to thermal equilibrium after we switched off the heating source. But with extrapolation it can be seen that the temperatures would return to their initial state after $\tau_{observed} = 27$ minutes. This data can be used to determine the value of the film coefficient of the BS, which was used in the previous section. We just have to modify equation 2.16 from chapter 2.3:

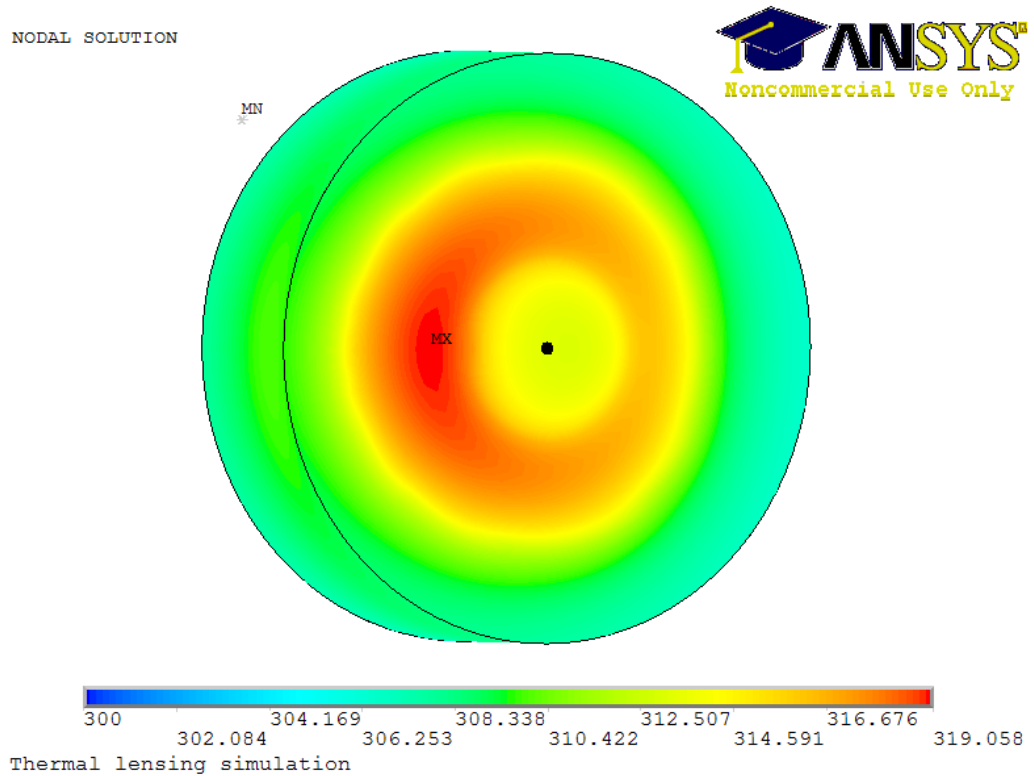
$$\tau_{observed} = \frac{Cm_{BS}}{(\text{radiative cooling rate})+(\text{convective cooling rate})} \quad (5.4)$$

$$= \frac{Cm_{BS}}{(4A\sigma T_0^3) + (hA)} \Rightarrow h \approx 34 \text{ W/m}^2\text{K} \quad (5.5)$$

With that it is clear that the effect of air is the dominant one.



(a) Temperature distribution of the BS as seen by an IR camera. Please note that this picture was taken in air.



(b) Simulated temperature in the beam splitter for the wide pattern.

Figure 5.8: Thermography and simulation of the temperature on the heated BS face.

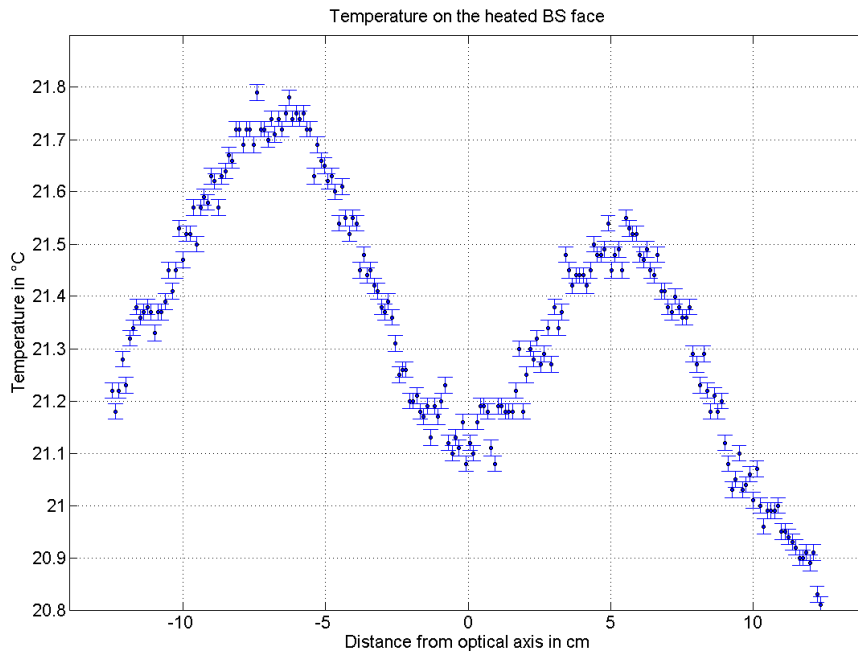


Figure 5.9: Temperature profile of the heated beam splitter front in horizontal direction, derived from the IR picture.

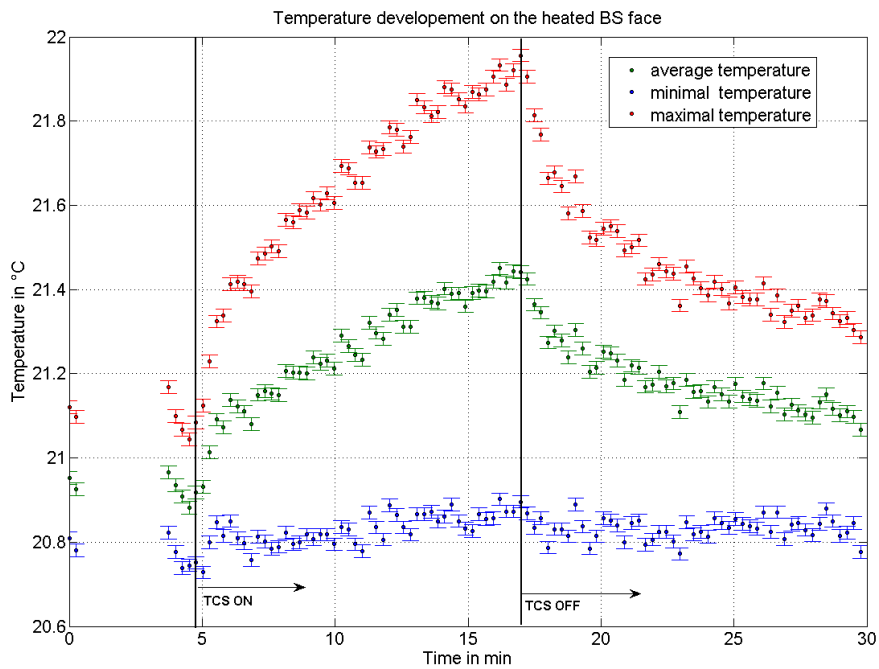


Figure 5.10: Temperature variation over time of the minimum, maximum and average temperature of the heated beam splitter side.

Chapter 6

Conclusion and future Prospects

6.1 Conclusion

A thermal compensation system for the GEO beam splitter has been developed. After evaluating different possibilities of compensating the thermal lens in the beam splitter, a compensation system based on thermal radiation was chosen to directly heat the beam splitter. Due to limited space in the vacuum tank, the whole system needs to be placed outside of the vacuum tank. An upper limit for the additional noise caused by the TCS has been derived, and found to be 10 times less than the targeted GEO-HF sensitivity at 1 kHz. The shape of the heating has been optimized using a genetic algorithm and finite elements modeling. These simulations also show, that the thermal compensation system is needed to reach a circulating light power of 20 kW. A test compensation system has been built. The simulated heating patterns can be created with the test system. Moreover, the heating patterns do transform into a temperature distribution in the beam splitter, as found by an infrared camera. The simulated temperatures could not be reached though, partly because of the effect of air. However, increasing the power of the prototype compensation system should be straight forward. The thermal compensation system will play an important role in the power upgrade of GEO-HF.

6.2 Future Prospects

The next step is the implementation of the compensation system in GEO-HF. A control system would be developed to adjust the power of the compensation system, and to switch it to central heating if necessary. For this, a suitable error signal needs to be determined.

If found to be necessary, the available heating power can be increased by a more efficient

coiling, gold coated mirrors, or by replacing the smaller parabolic mirror by a spherical one.

The long term stability of the TCS is crucial for science runs and should be investigated. Heating the Kanthal wire over a longer term might change its properties, especially the emissivity and the resistance, like shown in [ABT01]. Also oxidation of the aluminum mirrors might change the output power of the compensation system.

Bibliography

- [A⁺09] B P Abbott et al. LIGO: the Laser Interferometer Gravitational-Wave Observatory. *Reports on Progress in Physics*, 72(7):076901 (25pp), 2009.
- [AAA⁺08] F. Acernese, M. Alshourbagy, P. Amico, F. Antonucci, S. Aoudia, KG Arun, P. Astone, S. Avino, L. Baggio, G. Ballardin, et al. Virgo status. *Classical and Quantum Gravity*, 25:184001, 2008.
- [ABT01] H. Al-Badairy and GJ Talock. Oxidation mechanisms in high-temperature FeCrAl (RE) alloys. *Electrochem. Soc. Proc.*, 2001.
- [All97] A.H. Alloys. KANTHAL® HANDBOOK. *The Kanthal Corporation*, pages 4–38, 1997.
- [Bal06] S.W. Ballmer. *LIGO interferometer operating at design sensitivity with application to gravitational radiometry*. PhD thesis, MASSACHUSETTS INSTITUTE OF TECHNOLOGY, 2006.
- [BS09] Bernard F. Schutz B.S. Sathyaprakash. Physics, astrophysics and cosmology with gravitational waves. *Living Reviews in Relativity*, 12(2), 2009.
- [Col07] The Virgo Collaboration. Advanced Virgo Conceptual Design Virgo Report VIR 042A 07. http://www.cascina.virgo.infn.it/advirgo/docs/Adv_Design.pdf, 2007.
- [Deg06] J. Degallaix. *Compensation of strong thermal lensing in advanced interferometric gravitational waves detectors*. PhD thesis, University of Western Australia, 2006.
- [DGP⁺] Jérôme Degallaix, H Grote, M Prijatelj, M Hewitson, S Hild, C Affeldt, A Freise, J Leong, H Lück, K Strain, H Wittel, B Willke, and K Danzmann. Commissioning of the tuned DC readout at GEO 600. To be submitted to JPCS.
- [DZJB06] J. Degallaix, C. Zhao, L. Juf, and D. Blair. Superiority of sapphire over silicon test masses regarding thermal noise and thermal lensing for laser interferometers with

transmissive optics. volume 32, pages 404–412. Institute of Physics Publishing, 2006.

- [FHL⁺04] A. Freise, G. Heinzl, H. Lück, R. Schilling, B. Willke, and K. Danzmann. Frequency-domain interferometer simulation with higher-order spatial modes. *Classical and Quantum Gravity*, 21(5):1067, 2004.
- [FHS⁺00] A. Freise, G. Heinzl, KA Strain, J. Mizuno, KD Skeldon, H. Lück, B. Willke, R. Schilling, A. Ruediger, W. Winkler, et al. Demonstration of detuned dual recycling at the Garching 30 m laser interferometer. *Physics Letters A*, 277(3):135–142, 2000.
- [G⁺08] H. Grote et al. The status of GEO 600. *Class. Quantum Grav.*, 25:114043, 2008.
- [GFM⁺04] H. Grote, A. Freise, M. Malec, G. Heinzl, B. Willke, H. Luck, KA Strain, J. Hough, and K. Danzmann. Dual recycling for GEO 600. *Classical and Quantum Gravity*, 21(5):473, 2004.
- [HCC⁺03] J. Harms, Y. Chen, S. Chelkowski, A. Franzen, H. Vahlbruch, K. Danzmann, and R. Schnabel. Squeezed-input, optical-spring, signal-recycled gravitational-wave detectors. *Physical Review D*, 68(4):42001, 2003.
- [Hel01] P. Hello. Compensation for thermal effects in mirrors of gravitational wave interferometers. *The European Physical Journal D-Atomic, Molecular, Optical and Plasma Physics*, 15(3):373–383, 2001.
- [HGH⁺07] S. Hild, H. Grote, M. Hewitson, H. Luck, JR Smith, KA Strain, B. Willke, and K. Danzmann. Demonstration and comparison of tuned and detuned signal recycling in a large-scale gravitational wave detector. *Classical and Quantum Gravity*, 24(6):1513–1524, 2007.
- [Hil09] Stefan Hild. private communication, 2009.
- [HLW⁺06] S. Hild, H. Lück, W. Winkler, K. Strain, H. Grote, J. Smith, M. Malec, M. Hewitson, B. Willke, J. Hough, et al. Measurement of a low-absorption sample of OH-reduced fused silica. *Applied optics*, 45(28):7269–7272, 2006.
- [HT75a] R.A. Hulse and J.H. Taylor. Discovery of a pulsar in a binary system. *Astrophys. J*, 195:L51–L53, 1975.

-
- [HT75b] R.A. Hulse and J.H. Taylor. Discovery of a pulsar in a binary system. *Astrophys. J.*, 195:L51–L53, 1975.
- [HV93] P. Hello and J.Y. Vinet. Simulation of thermal effects in interferometric gravitational-wave detectors. *Phys. Lett.*, pages 351–6, 1993.
- [JKKPD09] C. Justin Kamp, H. Kawamura, R. Passaquieti, and R. DeSalvo. Directional radiative cooling thermal compensation for gravitational wave interferometer mirrors. *Nuclear Inst. and Methods in Physics Research, A*, 2009.
- [K⁺08] K. Kawabe et al. Status of LIGO. In *Journal of Physics: Conference Series*, volume 120, page 032003. Institute of Physics Publishing, 2008.
- [KPJ07] R. Kitamura, L. Pilon, and M. Jonasz. Optical constants of silica glass from extreme ultraviolet to far infrared at near room temperature. *Applied Optics*, 46(33):8118–8133, 2007.
- [Kur06] K. Kuroda. The status of LCGT. *Classical and Quantum Gravity*, 23:S215–S221, 2006.
- [Law03] R.C. Lawrence. *Active wavefront correction in laser interferometric gravitational wave detectors*. PhD thesis, Massachusetts Institute of Technology, 2003.
- [LFG⁺04] H. Lück, A. Freise, S. Goßler, S. Hild, K. Kawabe, and K. Danzmann. Thermal correction of the radii of curvature of mirrors for GEO 600. *Classical and Quantum Gravity*, 21(5):985, 2004.
- [LOZF04] R. Lawrence, D. Ottaway, M. Zucker, and P. Fritschel. Active correction of thermal lensing through external radiative thermal actuation. *Optics letters*, 29(22):2635–2637, 2004.
- [MHG⁺01] J.D. Mansell, J. Hennawi, E.K. Gustafson, M.M. Fejer, R.L. Byer, D. Clubley, S. Yoshida, and D.H. Reitze. Evaluating the effect of transmissive optic thermal lensing on laser beam quality with a Shack-Hartmann wave-front sensor. *Applied Optics*, 40(3):366–374, 2001.
- [Mit98] M. Mitchell. *An introduction to genetic algorithms*. The MIT press, 1998.
- [MSN⁺93] J. Mizuno, KA Strain, PG Nelson, JM Chen, R. Schilling, A. Rüdiger, W. Winkler, and K. Danzmann. Resonant sideband extraction: a new

- configuration for interferometric gravitational wave detectors. *Phys. Lett. A*, 175(5):273–276, 1993.
- [MTW⁺73] Charles W. Misner, Kip S. Thorne, John Archibald Wheeler, John Wheeler, and Kip Thorne. *Gravitation (Physics Series)*. W. H. Freeman, 2nd printing edition, 9 1973.
- [Mue08] M.A.A.G. Mueller. Design of the Advanced LIGO recycling cavities. *Opt. Express*, 16:10018–10032, 2008.
- [Sau94] Peter R. Saulson. *Fundamentals of Interferometric Gravitational Wave Detectors*. World Scientific Pub Co Inc, 11 1994.
- [Sch03] Bernard Schutz. *Gravity from the Ground Up: An Introductory Guide to Gravity and General Relativity*. Cambridge University Press, 1 edition, 11 2003.
- [Sch09] Bernard Schutz. *A First Course in General Relativity*. Cambridge University Press, 2nd edition, 6 2009.
- [SDM⁺94] KA Strain, K. Danzmann, J. Mizuno, PG Nelson, A. Rüdiger, R. Schilling, and W. Winkler. Thermal lensing in recycling interferometric gravitational wave detectors. *Physics Letters-Section A*, 194(1):124–132, 1994.
- [Sha08] DA Shaddock. Space-based gravitational wave detection with LISA. *Classical and Quantum Gravity*, 25(11):114012–114012, 2008.
- [Sie86] A. E. Siegman. *Lasers*. University Science Books, 1 1986.
- [Spe08] Tilo Sperling. Kompensation der thermischen Linse im GEO600 Strahlteiler - Semesterarbeit, 2008.
- [SS84] H. Sankur and W.H. Southwell. Broadband gradient-index antireflection coating for ZnSe. *Applied optics*, 23(16):2770–2773, 1984.
- [TAT⁺08] R. Takahashi, K. Arai, D. Tatsumi, M. Fukushima, T. Yamazaki, MK Fujimoto, K. Agatsuma, Y. Arase, N. Nakagawa, A. Takamori, et al. Operational status of TAMA300 with the seismic attenuation system (SAS). *Classical and Quantum Gravity*, 25(11):114036–114036, 2008.
- [Vah08] Henning Vahlbruch. *Squeezed Light for Gravitational Wave Astronomy*. PhD thesis, Gottfried Wilhelm Leibniz Universität Hannover, 2008.

- [Vin09] Jean-Yves Vinet. On special optical modes and thermal issues in advanced gravitational wave interferometric detectors. *Living Reviews in Relativity*, 12(5), 2009.
- [W⁺07] B. Willke et al. GEO600: status and plans. *Classical and Quantum Gravity*, 24(19):389, 2007.
- [WDG⁺07] W. Winkler, K. Danzmann, H. Grote, M. Hewitson, S. Hild, J. Hough, H. Lück, M. Malec, A. Freise, K. Mossavi, et al. The GEO 600 core optics. *Optics Communications*, 280(2):492–499, 2007.
- [WDRS91] W. Winkler, K. Danzmann, A. Rüdiger, and R. Schilling. Heating by optical absorption and the performance of interferometric gravitational-wave detectors. *Phys. Rev. A*, 44(11):7022–7036, Dec 1991.

Appendix A

Appendix

A.1 Genetic algorithm

Genetic algorithms (GAs) are a relatively new optimization method which works for global scale optimizations, originating from evolutionary computing. The GA resembles natural evolution and involves random processes. Genetic algorithms are usually used for “expensive” functions with many variables, where other optimization methods would take too long to find the minimum. It must be noted that they usually do not find the exact position of the minimum, but a spot close to it in the solution space. GAs require a “fitness function”, which returns a figure of merit (“fitness value”). It describes how good a solution is, a lower fitness value indicates a better solution. Usually it is the expensive part to calculate the fitness value. The fitness function is computed for a given set of input parameters (“individual”). The input parameters are called “chromosomes.” The GA usually starts with a random population of individuals. Then the fitness of each individual is calculated using the fitness function. In order to build the next generation, a selection process follows. It is a stochastic process, in which the fittest individuals are more likely to be selected. This randomness is necessary to keep the diversity up, preventing the algorithm from premature convergence to local optima, instead of finding the global one. Three operators are applied to the selected individuals to build the next generation of individuals:

1. Migration

The selected individuals (or some of them) are transferred into the next generation. This assures that the best solution of each generation is as good (or nearly as good, depending on the selection) as the best solution of the last generation.

2. Mutation

In the process of mutation some of the properties of each individual (“chromosomes”) are changed randomly. Then this new individual is passed into the next generation.

3. Recombination

in the recombination, chromosomes from one selected individual are combined with some chromosomes from another selected individual to create a new one. This new individual is then passed into the next generation.

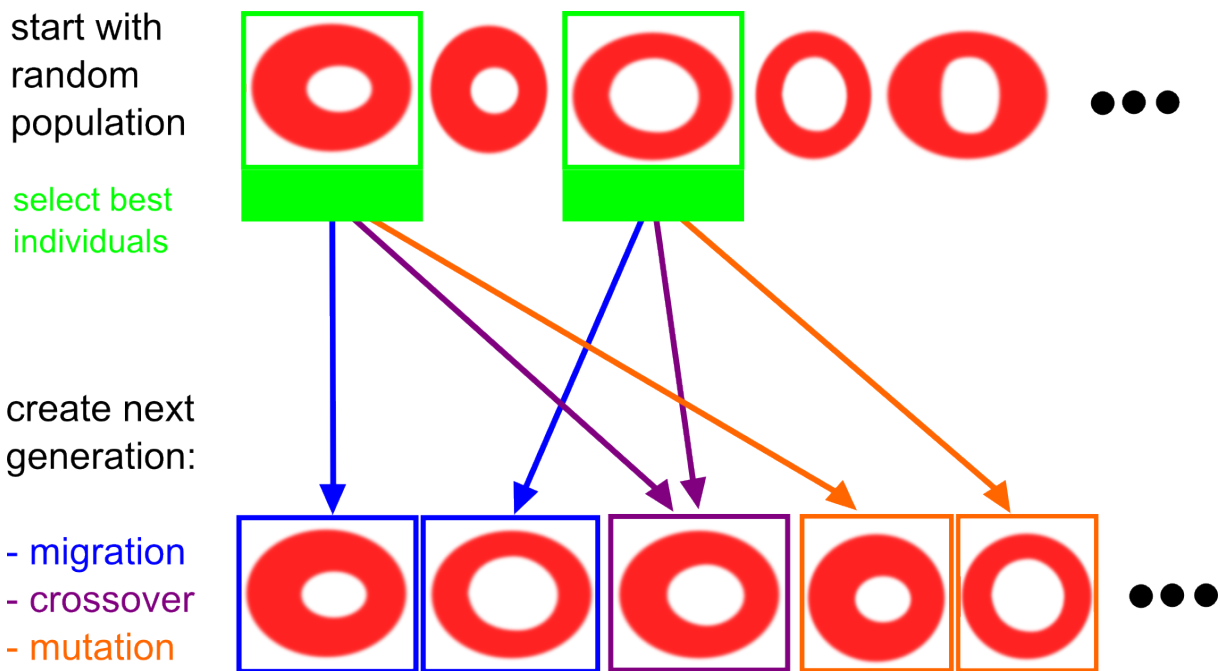


Figure A.1: Visualization of the working principle of a genetic algorithm.

Fig. A.1 visualizes this process. The algorithm continues the selection process for the current generation and builds following generations until a an abortion criterium is met. One criterium could be, that a maximum number of generations is reached, or that a solution is found that satisfies a certain criterium. The advantage of GAs lies in their nature to often quickly allocate global solutions of good fitness, especially on difficult or unknown search spaces. However, they do not usually return the exact position of the optimum. That is, why it is often useful to further optimize the result of the GA, with a Newton algorithm for example. This approach is called “hybrid optimization.”

A.2 ABCD Matrices to calculate the Beam Waist Size

The laser coming from the PR mirror has an angle of $\gamma_1 = 43^\circ$ to the surface normal of the beam splitter BS surface. Snell's law can be used to calculate the angle $\gamma_2 = 28^\circ$ between the surface normal and the laser inside the beam splitter. This leads to complications in terms of thermal lensing: inside the BS, the beam radius in the horizontal direction differs from the radius in vertical direction. This can be shown by the ABCD matrix formalism [Sie86]. The ABCD matrix for the beam in x direction looks like the following (from [Sie86], angle of incidence $\gamma_{1,2}$):

$$\begin{pmatrix} \frac{\cos(\gamma_2)}{\cos(\gamma_1)} & 0 \\ 0 & \frac{\cos(\gamma_1)}{\cos(\alpha_2)} \end{pmatrix} \quad (\text{A.1})$$

While in the y direction the beam waist is not changed:

$$\begin{pmatrix} 1 & 0 \\ 0 & 1 \end{pmatrix} \quad (\text{A.2})$$

The Gaussian beam parameter in the BS $q_2 = \frac{Aq_1+B}{Cq_1+D}$ can be calculated for both cases, q_1 is the beam parameter outside of the BS: $q_{2x} = \frac{Aq_{1x}+B}{Cq_{1x}+D} = \left(\frac{\cos(\gamma_1)}{\cos(\gamma_2)}\right)^2 q_{1x}$ And for the vertical direction: $q_{2y} = q_{1y}$

Now it is possible to build the quotient (assuming that the beam parameters and q_{1x} and q_{1y} outside of the beam splitter are equal)

$$\frac{q_{2x}}{q_{2y}} \approx \left(\frac{\cos(\gamma_1)}{\cos(\gamma_2)}\right)^2 \quad (\text{A.3})$$

We can use the relation

$$\frac{1}{q} = \frac{1}{R} - i \frac{\lambda/n}{\pi w^2}. \quad (\text{A.4})$$

where $1/R$ can be approximated with zero, since the beam has a waist near the power recycling mirror. If we put A.4 into A.3 with $\gamma_1 = 43^\circ$ and $\gamma_2 = 28^\circ$ we get to a difference between the both directions of a factor ≈ 1.2 .

A.3 Tables for the Compensation Patterns

	2.7 kw no comp	2.7 kw w comp	20 kw no comp	20 kw w comp
f_x	8031 m	-45066 m	1084 m	26945 m
f_y	5835 m	47592 m	788 m	2359 m
sc. loss	$4 \cdot 10^{-4}$ W	$3.9 \cdot 10^{-5}$ W	$2.4 \cdot 10^{-2}$ W	$2 \cdot 10^{-3}$ W

Table A.1: Table with values for a narrow pattern.

	2.7 kw no comp	2.7 kw w comp	20 kw no comp	20 kw w comp
f_x	8031 m	95884 m	1084 m	2855 m
f_y	5835 m	26150 m	788 m	1860 m
sc. loss	$4 \cdot 10^{-4}$ W	$2.3 \cdot 10^{-5}$ W	$2.4 \cdot 10^{-2}$ W	$4 \cdot 10^{-3}$ W

Table A.2: Table with values for a wide pattern.

	2.7 kw no comp	2.7 kw w comp	20 kw no comp	20 kw w comp
f_x	8031 m	66420 m	1084 m	5881 m
f_y	5835 m	25389 m	788 m	2763 m
sc. loss	$4 \cdot 10^{-4}$ W	$2.5 \cdot 10^{-5}$ W	$2.4 \cdot 10^{-2}$ W	$4.5 \cdot 10^{-3}$ W

Table A.3: Table with values for both sides heating.

	2.7 kw no comp	2.7 kw w comp	20 kw no comp	20 kw w comp
f_x	8031 m	$-1.8 \cdot 10^6$ m	1084 m	6762 m
f_y	5835 m	-47572 m	788 m	4900 m
sc. loss	$4 \cdot 10^{-4}$ W	$3.4 \cdot 10^{-5}$ W	$2.4 \cdot 10^{-2}$ W	$1.6 \cdot 10^{-3}$ W

Table A.4: Table with values for back side heating.

A.4 Parameters for the found heating Patterns

	$x_{o-off.}$	$y_{o-off.}$	x_{o1}	x_{o2}	y_o	$x_{i-off.}$	$y_{i-off.}$	x_{i1}	x_{i2}	y_i
narrow	1.6	0	7.5	7.4	6.5	0.9	0	2.2	2.1	2.0
wide	0.0	0	10	7.6	8.6	0.0	0	3.9	3.6	4.0
both s.	2.9	0	7.1	7.1	7.1	2.9	0	5.1	4.1	4.4
backside	4.0	0	6.3	6.4	6.4	4.7	0	3.7	3.7	4.0

Table A.5: Table with values for the heating patterns. All values are given in cm. The columns give the parameters as defined by fig. 4.5.

A.5 Transmission Spectrum of the IR Fresnel Lens

The transmission spectrum was taken from http://www.fresneltech.com/graphs/polyir2_graph.html.

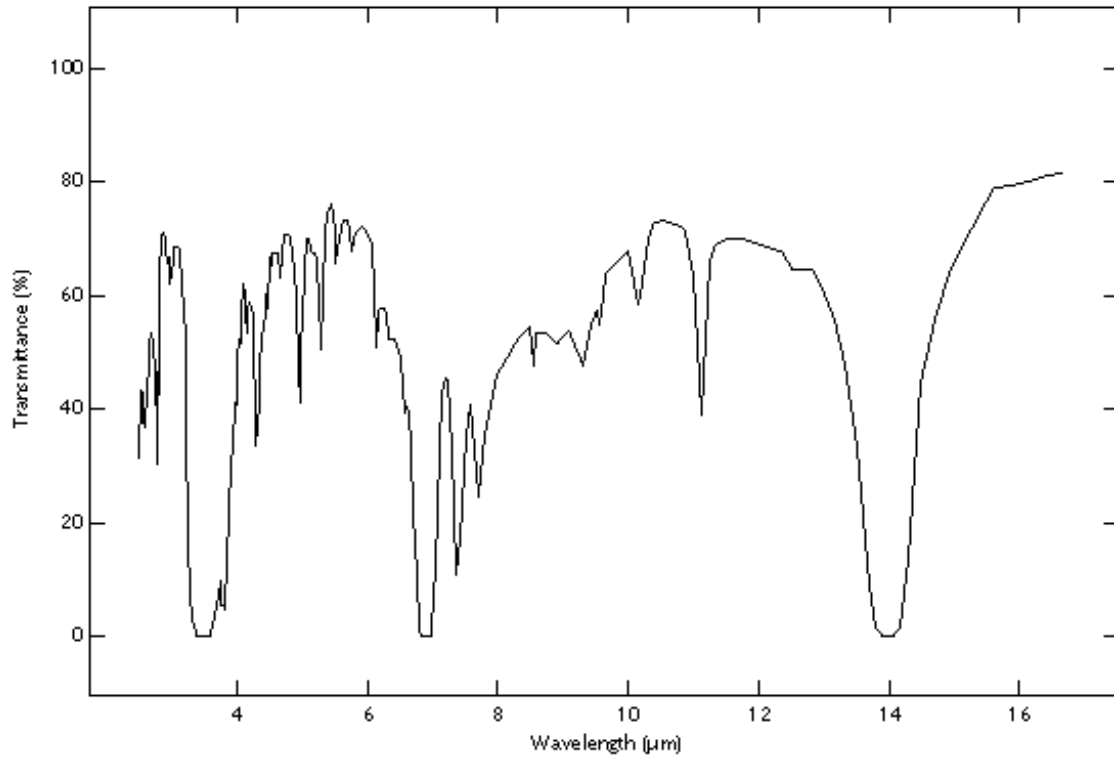


Figure A.2: Transmission spectrum of the IR Fresnel lens.

A.6 Example Scripts

For the completeness of this work, there are two scripts appended:

- an example ANSYS script which calculates the temperature and displacement for every point in the BS if supplied with the absorbed power of heating pattern and laser beam for each point
- an example Finesse script which computes the effect of the compensation on the interferometer as a whole, using a modified version of the “official” GEO 600 FINESSE-script

A.6.1 ANSYS Script

```
! Thermal lensing script by Jerome Degallaix , 2007
FILENAME,TM_TL104,0
/TITLE, Thermal lensing simulation
/UNITS, SI

!----- Definition -----
Diam_cyl      = 0.26      ! Diameter of the test mass
Length_cyl    = 0.08      ! Length of the test mass
Troom         = 300       ! Temperature of the room
Mesh_div      = 25        ! For the meshing of the thickness , number of division
Rad_cyl = Diam_cyl/2

!Thermal and structure test
/NOPR
/PMETH,OFF,0
KEYW,PR_SET,1
KEYW,PR_STRUC,1
KEYW,PR_THERM,1
/GO

/PREP7
SHPP,MODIFY,1,30
! Element type
ET,2,SOLID70,
ET,3,SURF152,,,1,1
KEYOPT,3,9,1      ! RADIATION OPTION
R,3,1,0.568E-7    ! FORM FACTOR = 1, STEFAN-BOLTZMANN CONSTANT
MP,EMIS,3,1      ! BLACK BODY EMISSIVITY

! Material 1 = Fused silica
MP,DENS,1,2202    ! Density
MP,EX,1,7.3E+010  ! Young modulus
MP,PRXY,1,0.17    ! Poisson ratio
MP,ALPX,1,0.55e-6 ! Thermal expansion
MP,KXX,1,1.38     ! Thermal conductivity
MP,C,1,740        ! Specific heat

! Define and mesh the base
CYL4,0,0,0,0, Rad_cyl,90, Length_cyl
CYL4,0,0,0,90, Rad_cyl,180, Length_cyl
CYL4,0,0,0,180, Rad_cyl,270, Length_cyl
CYL4,0,0,0,270, Rad_cyl,360, Length_cyl
VGLUE,1,2,3,4
MSHKEY,1
ESIZE,, Mesh_div
```

A Appendix

```
VSWEEP,6,28,5
VSWEEP,1,5,4
VSWEEP,5,4,24
VSWEEP,7,24,28,

TYPE,3
REAL,3
MAT,3
N,250000,0.1,0.1,0.1      ! EXTRA "SPACE" NODE FOR RADIATION
ESURF,250000              ! GENERATE SURF152 ELEMENTS

/SOLU

VFOPT,none
ANTYPE,0

!----- Apply conditions -----
*dim,LOAD_HEAT,table,151,151,51,x,y,z,
*tread,LOAD_HEAT,Abs_data104,txt
VSEL,S,VOLU,,1,1
VSEL,A,VOLU,,6,6
VSEL,A,VOLU,,7,7
VSEL,A,VOLU,,5,5
BFV,ALL,HGEN,%LOAD_HEAT%

ASEL,S,AREA,,1,1
ASEL,A,AREA,,21,21
ASEL,A,AREA,,29,29
ASEL,A,AREA,,25,25
SFA,ALL,1,HFLUX,

ASEL,ALL
SFA,ALL,,RDSF,1,1,
TOFFST,0
SPCTEMP,1,Troom

!----- Option -----
OUTPR,ALL,NONE,
OUTRES,NSOL,LAST,
AUTOTS,1
KBC,1
NSUBST,10,,1
TREF,Troom,
D,250000,TEMP,Troom      ! SPECIFY SURROUNDING ABSOLUTE TEMPERATURE
SBCTRAN
EQSLV,JCG,1E-5
/STATUS,SOLU
SOLVE

/GRAPHICS,POWER
/EFACET,4
AVRES,1,FULL
FINISH

*get,NCOUNT,node,,count      ! Get total number of selected nodes
*dim,NARRAY,array,NCOUNT,7   ! Create NCOUNT x 7 array

*vget,NARRAY(1,4),node,1,temp ! Fill temperature profile

! now the mechanical part
/PREP7
SFADELE,all,,RDSF
ETCHG,TTS
KEYOPT,2,2,3
FINISH
EQSLV,JCG,1E-5,
/SOLU
OUTPR,ALL,NONE,
OUTRES,NSOL,LAST,
ANTYPE,0
```

```
LDREAD,TEMP,,,,test104,rth,
/STATUS,SOLU
SOLVE
FINISH
```

```
/post1
set,last
*cfopen,data_T104,txt
*vget,NARRAY(1,1),node,1,loc,x           ! Fill first column with x-location
*vget,NARRAY(1,2),node,1,loc,y           ! Fill second column with y-location.
*vget,NARRAY(1,3),node,1,loc,z           ! Fill third column with z-location.
*vget,NARRAY(1,5),node,1,U,X             ! Fill displacement profile
*vget,NARRAY(1,6),node,1,U,Y             ! Fill displacement profile
*vget,NARRAY(1,7),node,1,U,Z             ! Fill displacement profile
*vwrite,NARRAY(1,1),NARRAY(1,2),NARRAY(1,3),NARRAY(1,4),NARRAY(1,5),NARRAY(1,6),NARRAY(1,7) ! Write columns to file
(E13.5,2X,E13.5,2X,E13.5,2X,E13.7,2X,E13.7,2X,E13.7,2X,E13.7) ! Format with decimal and scientific
FINISH
```

A.6.2 Example Finesse Script

```
#-----
# geo600-main.kat $Rev: 42 $ ----- modified! for use with finesse pre 0.98
# Andreas Freise (adf@star.sr.bham.ac.uk)
# $Date: 2007-09-11 16:23:08 +0100 (Tue, 11 Sep 2007) $
#
# (Modified by Holger Wittel, 2009)
#
# Input File for FINESSE (www.rzg.mpg.de/~adf)
#
# Optical layout of GEO 600 with "real" parameters .
#-----

%%% FTblock constants
const maxtem 6
const phimin -40
const phimax 40
const phisteps 120
const pmax 2
const pmin 40
const psteps 100
const phiMCE 0
%%% FTend constants

%%% FTblock first
#-----
## Laser bench ##

# Laser
# (distances on laser bench up to MMCla are only approximately)
l i1 4.82 0 nLaser # power injected into MCl (for 75deg, see page 3984)
# Relation between injected power and tuning in [deg]:
# [deg] [W]
# 70 : 3.47
# 75 : 4.82 (ratio 1.39 to 70Deg.)
# 80 : 6.1
# 85 : 7.12
# 94 : 8.05
# 95 : 8.07

gauss beam_in i1 nLaser lm -5.4
# beam size that fits into MCl, we assume "i1" includes the laser and
# mode matching lense as well as all the other components from the
# laser bench, except the modulator and the last table mounted mirror.

s s0 1 nLaser nEOMlin

## MU 1, modulation for PDH for locking laser to MCl
mod eom1 25M 0.1 1 pm 0 nEOMlin nEOM1out ## MCl PDH locking frequency

s s1 1 nEOM1out nZ1
bs mZ 1 0 0 nZ1 nZ2 dump dump # the last table mounted mirror
s s2 2.86 nZ2 nBDIMCla

#-----
## mode cleaners ##
#
# The mode cleaners are rougly adapted to fit the measured
# visibility, throughput or finesse, see labbok 4027

## MCl
bs1 BDIMCl 50u 30u 0 45 nBDIMCla nBDIMClb dump dump
s mc1_sin 0.45 nBDIMClb nMClin
bs1 MMCla 1240u 130u 0 44.45 nMClin nMCl1refl nMCl0 nMCl5
s mc1_s0 0.15 nMCl0 nMCl1
bs1 MMClb 35u 130u 0.0003 2.2 nMCl3 nMCl4 dump dump #3*10-10m away from res.
attr MMClb Rc 6.72
s mc1_s1 3.926 nMCl4 nMCl5
bs1 MMClc 1240u 130u 0 44.45 nMCl1 nMCl2 nMClout dump
s mc1_s2 3.926 nMCl2 nMCl3
```

```

s smcme1 0.5 nMC1out nMU2in
## MU 2
mod eom2 13M .1 1 pm 0 nMU2in nMU2_1      # MC2 PDH locking frequency
mod eom3 $fPR $midxPR 1 pm 0 nMU2_1 nMU2_2  # PRC PDH locking frquency
isol d1 0 nMU2_2 nMU2out                   # Faraday Isolator
s      smcme2 0.5 nMU2out nMC2in

## MC2
bs1 MMC2a 1000u 130u 0 44.45 nMC2in nMC2refl nMC2_0 nMC2_5
s      mc2_s 0.15 nMC2_0 nMC2_1
# inner surface of MMC2b:
bs1 MMC2bi 1000u 130u 0 2.2 nMC2_3 nMC2_4 nMC2bi dump
attr MMC2bi Rc 6.72
s      mc2_s1 3.9588 nMC2_4 nMC2_5
bs1 MMC2c 114u 130u 0.0003 44.45 nMC2_1 nMC2_2 dump dump #3*10^-10m away from res.
s      mc2_s2 3.9588 nMC2_2 nMC2_3

s      sMMC2b 0.05 1.44963 nMC2bi nMC2bo
# second surface of MMC2b:
m      MMC2bo 0 1 0 nMC2bo nMC2out
attr MMC2bo Rc 0.35

s      smcpr1 0.135 nMC2out nBDMC2a
bs1 BDMC2 50u 30u 0 45 nBDMC2a nBDMC2b dump dump

# Note:
# The length of 'smcpr2' and 'smcpr3' represent not the geometrical
# distance but the length of the space with respect to mode propagation.
# The values include the effects of the Faraday crystals and the
# modulator crystals which are not explicitelty given here.

# 070502 corrected length with respect to OptoCad (Roland Schilling)
s      smcpr2 0.2825 nBDMC2b nMU3in

mod eom4 $fSR $midxSR 2 pm 0 nMU3in nMU3_2   # Schnupp1 (SR control)
mod eom5 $fMI $midxMI 2 pm 0 nMU3_2 nMU3_3   # Schnupp2 (MI control)

lens lpr 1.8 nMU3_3 nMU3_4
# some rather arbitrary thermal lense for the isolators and the EOMs:
lens therm 5.2 nMU3_4 nMU3_5                # ** to be checked **
isol d2 120 nMU3_5 nMU3out                   # Faraday Isolator

# 070502 corrected length with respect to OptoCad (Roland Schilling)
s      smcpr3 4.391 nMU3out nBDIPR1
bs1 BDIPR 50u 30u 0 45 nBDIPR1 nBDIPR2 dump dump
s      smcpr4 0.11 nBDIPR2 nMPR1

#####
## main interferometer ##
##
## New MPR; values for MPR005 page 2264 (check with Harald)
## first (curved) surface of MPR
m      mPRo 0 1 0 nMPR1 nMPRi1
attr mPRo Rc -1.85
s      smpr 0.0718 1.44963 nMPRi1 nMPRi2
# second (inner) surface of MPR
m1     MPR 900u SLMPR 0. nMPRi2 nMPR2        # T=900 ppm, L=50 ppm

s      swest 1.1463 nMPR2 nBSwest             # new length with T_PR=900 ppm ** to be checked **

#####
## BS
## basic data from old GEO files
##
##
##          nBSnorth      ,'-
##          |      +      '
##          |      ,      '
##          |      +i1      +
##          nBSwest      +i1      +
##          ----->      ,'- i2 ,'

```

A Appendix

```
##          + \ ' - , +          nBSeast
##          , ' i3 \ , ' -----
##          +          \ +
##          , '          i4 , '
##          ' - , ' | nBSsouth
##          - |
##          |
##          |
bs2  BS 0.485998 $LBS 0.0 42.834 nBSwest nBSnorth nBSi1 nBSi3

s  sBS1a 0.040 1.44963 nBSi1 nBSi1b
##-----
# Thermal lens of beam splitter
lens bst 5000k nBSi1b nBSi1c # static value for 1.9kW at BS
##-----
# Alternative: dynamic thermal lens computation, as in:
# S. Hild et al, Applied Optics IP, vol. 45, Issue 28, pp.7269-7272
# assuming 0.25ppm/cm absorption, w=0.88cm, d=9cm
/*
pd prcpower nBSwest # we need 2* power in BS, so we measure power in west arm
noplots prcpower
set bspow prcpower re
func flength = 1.6635E7 / ( $bspow + 0.0000000001)
#noplots flength
put bst f $flength
*/

s  sBS1 0.051 1.44963 nBSi1c nBSi2
s  sBS2 0.091 1.44963 nBSi3 nBSi4
bs2 BS2 60u $LSAR 0 27.9694 nBSi2 dump nBSeast nBSAR # R=60 ppm, L=30ppm
bs2 BS3 60u $LSAR 0 -27.9694 nBSi4 dump nBSsouth dump # R=60 ppm, L=30ppm

#####
#####
## Astigmatic lens, represented by two mirrors, one with curvature in x and y direction
## based on an absorption of 0.5 ppm and a beta of 0.9

s beforeTL 1n nBSeast nMITHERM1
m MITHERM1 0 1 0 nMITHERM1 nMITHERM2
s STHERM 1n 2 nMITHERM2 nMITHERM3 #not so sure about this one

m MITHERM2 0 1 0 nMITHERM3 nBSeast0
attr MITHERM2 Rcx 9E15k
attr MITHERM2 Rcy 9E15k

##calculate and set the radii of curvature for focal lengths
#func timespower=$x1/3.47
## noplots timespower
#func fthermx=6642/$timespower
#func fthermy=5734/$timespower

pd BSpow2 nBSwest
set power BSpow2 re
#func fthermx=17933400/($power +1.0E-15)
#func fthermy=15481800/($power +1.0E-15)

#func RX= ((1))*$fthermx
#func RY= ((1))*$fthermy

#noplots fthermx
#noplots fthermy

#noplots RX
#noplots RY

#put MITHERM2 Rcx $RX
#put MITHERM2 Rcy $RY
```

```

### mirror for the phasemap with T=1
s SphaseM 1n nBSeast0 nMphaseM
m MphaseM 0 1 0 nMphaseM nbetw1
s betw 1n 2 nbetw1 nbetw2
m MphaseM2 0 1 0 nbetw2 nbetw3
s betw2 1n 1 nbetw3 nbetw4
lens testlens -2000E15 nbetw4 nBSeast1

#####

#####

#####
##check the gain of the PRC
#pd MPRin nMPR1*
set MPRinpow MPRin re
noplots MPRin
func PRCgain=$power/($MPRinpow+ 1E-15)
#####

#####
##darkport / intracav
pd darkport nout
noplots darkport
set dark darkport re
func dark / west=$dark / ($power + 1E-15)
#####
%%FTend first

%%FTblock phasemap
#####
##PHASEMAP for compensation
map MphaseM 0 trans_map202.txt
savemap MphaseM bs_trans_map trans_map202.txt
debug 64
#####
%%FTend phasemap

%%FTblock second
#-----
## north arm
s snorth1 598.5682 nBSnorth nMFN1 # ** to be checked **

bs1 MFN 8.3u $LMFN 0.0 0.0 nMFN1 nMFN2 dump dump # T=8.3 ppm
attr MFN Rc 666

s snorth2 597.0241 nMFN2 nMCN1 # ** to be checked **

m1 MCN 13u $LMCN -0.0 nMCN1 dump # T=13 ppm
attr MCN Rc 636

#-----
## east arm

s seast1 598.4497 nBSeast1 nMFE1
bs1 MFE 8.3u $LMFE 0.0 0.0 nMFE1 nMFE2 dump dump # T=8.3 ppm
# ** the Rc(T) below need to be checked, they certainly look wrong **
attr MFE Rcx 664 # 90 W
attr MFE Rcy 660 # 90 W

s seast2 597.0630 nMFE2 nMCE1
m1 MCE 13u $LMCE 0.0 nMCE1 dump # T=13ppm
m1 MCE 13u $LMCE $phiMCE nMCE1 dump # T=13ppm
attr MCE Rc 622

#-----
## south arm

```

A Appendix

```
s ssouth 1.109 nBssouth nMSR1

m MSR 0.9805 0.01945 0.79048 nMSR1 nMSR2      # R=0.9805, T=0.01945, L=50 ppm
# tuning = f_tune/FSR_SR * 180, FSR_SR=125241 Hz ** to be checked **
# e.g f_tune 532 Hz -> 0.7646 deg
# 550 Hz -> 0.79048 deg ???!
##-----
## output optics telescope

s sout1 1.8 nMSR2 nBDO1i
bs1 BDO1 0.01 0.0 0.0 5.0 nBDO1i nBDO1o dump dump # T=1%
attr BDO1 Rc 6.72

s sout2 4.855 nBDO1o nLO1i # BDO2 and BDO3 are flat and omitted in this path
lens LO1 0.5 nLO1i nLO1o # 1. lens on detection bench
s sout3 0.703 nLO1o nLO2i # computed telescope length, 2 flat mirrors omitted in this path
lens LO2 -0.03 nLO2i nLO2o # 2. lens on detection bench
# actual lens -0.05m ?
s sout4 1.0 nLO2o nout # length to quad. camera

##-----
## further settings and commands

# Modulation frquencies
const fSR 9016865 ## corresponding to 532 Hz on tune.vi, (10/2006 S. Hild)
const fMI 14.904929M ## (10/2006 S. Hild)
const fPR 37.16M
const midxPR 0.13 # see page 4011
const midxSR 0.17 # see page 4011
const midxMI 0.38 # see page 4011

# Michelson losses
# tuned to give approx 2.kW on BS
const LMPR 130u
const LMCN 130u
const LMFN 130u
const LMCE 130u
const LMFE 130u
const LBS 130u
const LBSAR 130u

# MC1 cavity
cav mc1 MMC1a nMC1_0 MMC1a nMC1_5
# MC2 cavity
cav mc2 MMC2a nMC2_0 MMC2a nMC2_5
# SR cavity (north arm)
cav src1 MSR nMSR1 MCN nMCN1
# SR cavity (east arm)
cav src2 MSR nMSR1 MCE nMCE1
# PR cavity (north arm)
cav pre1 MPR nMPR2 MCN nMCN1
# PR cavity (east arm)
cav pre2 MPR nMPR2 MCE nMCE1

##-----
## Simualtion commands

# power detectors
#pd MC1out nMU2_2
#pd MC2out nMU3_5
pd MPRrelf nMPR1
pd MPRin nMPR1*
pd PRC nMPR2
pd BSpow nBSwest
pd darkport nout
#xaxis BS phi lin -.03 .03 80

##-----

maxtem Smaxtem
#retrace off
```

```
time
phase 3
trace 10

pause
gnuterm windows
###
%%FTend second

%%FTblock command
xaxis MCE phi lin $phimin $phimax $phisteps
#xaxis i1 P lin $pmin $pmax $psteps

yaxis log abs
%%FTend command
```

A.7 Used Parameters

Parameter	symbol	value	unit
Speed of light	c	$3 \cdot 10^8$	m/s
reduced Planck const.	\hbar	$1.055 \cdot 10^{-34}$	Js
Boltzmann const.	k_B	$1.38 \cdot 10^{-23}$	J/K
Stefan-Boltzmann const.	σ	$5.67 \cdot 10^{-8}$	W/m ² K ⁴
ambient temperature	T_0	300	K
beam waist radius	ω	1	cm
beam waist radius x	ω_x	1.2	cm
beam waist radius y	ω_y	1	cm
path length in the BS	L	9	cm
Fused silica			
refractive index (at 1064 nm)	n	1.44963	—
thermo refractive coeff.	β	$9 \cdot 10^{-6}$	K ⁻¹
thermal conductivity	κ	1.38	W/mK
thermal expansion coefficient	α	$0.55 \cdot 10^{-6}$	K ⁻¹
specific heat	c	740	J/KgK
Absorption	p_{abs}	0.5	ppm/cm
Density	ρ	2202	kg/m ³
Poisson ratio		0.17	—
photoelastic coeff.	ρ_{12}	0.27	—

Table A.6: Table of used parameters.

Acknowledgements

This thesis would not have been possible without the help and support of several people.

First I want to thank Prof. Dr. Karsten Danzmann for giving me the opportunity of working in this Institute. I also want to thank all the members of the institute for contributing to the very friendly atmosphere.

A big 'Thank you' goes to the GEO group for a great time and lot of helpful discussions. Special thanks to Jérôme, Harald and Hartmut for guiding me and patiently answering my questions. For the correction of the thesis I want to thank Jérôme, Harald, Christoph and Mădă.

Thanks to Andrea Hildebrand for helping me out with the infrared camera.

I am thanking my parents, who always supported me.

Finally I want to thank my dear Mădălina for all the love and care.

Thank you!

Selbständigkeitserklärung

Hiermit versichere ich, dass ich diese Arbeit selbständig verfasst und keine anderen als die angegebenen Hilfsmittel und Quellen benutzt habe.

Holger Wittel
Oktober 2009